THE JOURNAL OF PHYSICAL CHEMISTRY B
A JOURNAL OF THE AMERICAN CHEMICAL SOCIETY

pubs.acs.org/JPCB Article

A Road Map to Various Pathways for Calculating the Memory Kernel of the Generalized Quantum Master Equation

Published as part of The Journal of Physical Chemistry virtual special issue "125 Years of The Journal of Physical Chemistry".

Ellen Mulvihill and Eitan Geva*

Cite This: *J. Phys. Chem. B* 2021, 125, 9834–9852 Read Online

ACCESS | Metrics & More | Article Recommendations | Supporting Information

ABSTRACT: The generalized quantum master equation (GQME) provides a powerful framework for simulating electronic energy, charge, and coherence transfer dynamics in molecular systems. Within this framework, the effect of the nuclear degrees of freedom on the time evolution of the electronic reduced density matrix is fully captured by a memory kernel superoperator. However, the actual memory kernel depends on the choice of projection operator and is therefore not unique. Furthermore, calculating the memory kernel can be done in multiple ways that use different forms of projection-free inputs. Although the electronic dynamics is invariant to those choices when quantum-mechanically exact projection-free inputs are used, this is not the case when they are obtained via more feasible semiclassical or mixed quantum-classical approximate methods. Furthermore, the accuracy and numerical stability of the resulting electronic dynamics has been observed to be sensitive to the above-mentioned choices when approximate methods are used to calculate the projection-free inputs. In this article, we provide a systematic road map to 30 possible pathways for calculating the memory kernel and highlight how they are related as well as the ways in which they differ. We also compare the performance of different pathways in the context of the spin-boson benchmark model, with the projection-free inputs obtained via a mapping Hamiltonian linearized semiclassical method. In this case, we find that expressing the memory kernel with an exponential operator where the projection operator precedes the Liouvillian yields the most accurate and most numerically stable results.

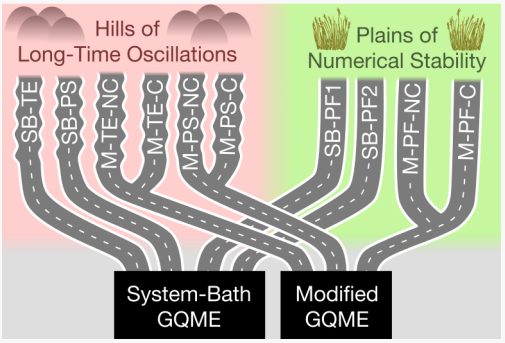

1. INTRODUCTION

A variety of important chemical processes, ranging from photosynthesis to photovoltaics, involve an intricate network of interrelated electronic energy, charge, and coherence transfer pathways.[1−12] The simulation of the inherently quantum-mechanical dynamics underlying these pathways remains one of the most formidable challenges facing computational chemistry. The exponential scaling of the computational cost with system dimensionality makes the quantum-mechanically exact simulation of such processes nonfeasible in complex molecular systems, with the exception of a subclass of Hamiltonians whose form makes such a quantum-mechanically exact simulation possible.[13−19]

The generalized quantum master equation (GQME) formalism, which was introduced by Nakajima[20] and Zwanzig[21] more than 60 years ago, provides a formal framework for deriving the exact equation of motion of an open quantum system. Describing electronic energy, charge, and coherence transfer in molecular systems via the GQME is based on treating the electronic degrees of freedom (DOF) as the quantum open system. This is accomplished by projecting out the nuclear DOF and accounting for their effect on the dynamics of the reduced electronic density matrix in terms of a memory kernel superoperator. The memory kernel superoperator, or its matrix representation in terms of the electronic basis of choice, corresponds to the minimal information about the nuclear DOF, which is needed in order to fully capture their effect on the electronic DOF. The matrix elements of the memory kernel typically represent electronic energy, charge, and coherence transfer rate coefficients, which are key for understanding function-structure relations as well as developing rational design principles in the aforementioned biologically and technologically relevant molecular systems.

Received: June 28, 2021
Revised: August 5, 2021
Published: August 23, 2021

https://doi.org/10.1021/acs.jpcb.1c05719
J. Phys. Chem. B 2021, 125, 9834–9852

Efforts over the last two decades have been directed at developing, testing, and applying computational methods for calculating the memory kernel, using either quantum-mechanically exact or approximate semiclassical and mixed quantum-classical methods.[22−40] The motivation for doing so comes from the fact that the memory kernel is often short-lived, which makes it possible to limit the use of exact or approximate methods to relatively short times, where they are often more accurate or more cost-effective or both. The short lifetime of the memory kernel combined with its scaling with the number of electronic states ($\sim N_e^4$, where N_e is the number of electronic states[22]) makes the GQME approach most beneficial for systems with a small number of electronic DOF and a memory time that is too long for weak coupling to be valid but shorter than the time scale of system dynamics.

The various computational schemes for calculating the memory kernel under consideration in this article are all based on the fact that the memory kernel can be obtained from projection-free inputs by solving integral Volterra equations, as was first shown by Shi and Geva in ref 22. Shi and Geva also demonstrated the feasibility and usefulness of this approach by calculating the memory kernel for the spin-boson model from quantum-mechanically exact projection-free inputs,[22] as well as from inputs obtained via an approximate semiclassical method.[23] Using semiclassical projection-free inputs, Shi and Geva also calculated the memory kernel for an anharmonic model of a two-level atom coupled to a chain of Lennard-Jones atoms.[23]

The Shi−Geva approach was later extended and streamlined by Zhang, Ka, and Geva in a manner that made it possible to account for a wider class of projection operators and initial conditions.[24] The Zhang−Ka−Geva approach was also used to calculate the memory kernel for an atomistic model of a two-state chromophore in liquid solution and to study the sensitivity of photon echo signals to the heterogeneity and non-Markovity of the underlying solvation dynamics.[25]

Rabani and co-workers have calculated the memory kernel of a quantum dot with electron-phonon interaction[27] and the Anderson impurity model[26,28,29,31] from quantum-mechanically exact projection-free inputs within the Zhang−Ka−Geva approach and introduced a method for calculating the memory kernel from the reduced system propagator.[36] The Shi−Geva and Zhang−Ka−Geva approaches were further explored and extended by Montoya-Castillo and Reichman, who introduced new forms of calculating the projection-free inputs.[33]

Markland and co-workers proposed calculating the memory kernel from projection-free inputs obtained via suface hopping[30] and the Ehrenfest mean-field method[34] within the Shi−Geva approach. By applying this scheme to the spin-boson model, they demonstrated how limiting the use of the Ehrenfest method to calculating the projection-free inputs produced significantly more accurate results in comparison to the direct application of the Ehrenfest method. Additional applications of this scheme to an atomistic model of charge transfer in water[32] and photosynthetic light harvesting systems[37] provided additional demonstrations for the benefits of limiting the use of the Ehrenfest method to calculating the projection-free inputs within the Shi−Geva approach. Markland and co-workers also explored the conditions that would need to be satisfied in order for the Shi−Geva and Zhang−Ka−Geva approaches to yield improved results compared to direct application of the approximate method.[35]

More recently, a modified form of the GQME and protocols for calculating the corresponding memory kernel were introduced by Mulvihill et al.[38] Unlike the previous implementations, this modified GQME approach did not require casting the Hamiltonian in a system-bath form and was found to yield more numerically stable results when combined with various approximate input methods on both the spin-boson model and the Fenna−Matthews−Olson (FMO) complex.[38−40]

In this article, we provide a systematic road map to 30 different pathways for calculating the memory kernel of the GQME. Among those 30 pathways are previously reported ones as well as new ones. The road map is designed in a manner that highlights the relationships between different pathways as well as the ways in which they differ. We also provide a comprehensive analysis of the performance of the different pathways in the context of the spin-boson benchmark model with the projection-free inputs obtained via a mapping Hamiltonian linearized semiclassical (LSC) method. In this case, we find that the biggest factor in determining the accuracy and numerical stability of a pathway is the order in which the projection operator and Liouvillian appear in the exponential operator within the memory kernel, where having the projection operator precede the Liouvillian yields the most accurate as well as most numerically stable results.

The rest of this article is organized as follows. We start out by presenting and discussing several preliminary considerations in section 2.1. Two different types of GQME, namely, the *system-bath GQME* and the *modified GQME*, are described in section 2.2. Different representations of the memory kernel of the system-bath and modified GQMEs are described in section 2.3. The various approaches to obtain the memory kernel are outlined in section 2.4. Different forms of the projection-free inputs are outlined in section 2.5. The results of applying each of the pathways to the spin-boson model are reported in section 3 and discussed in section 4. Concluding remarks are given in section 5. Technical aspects are detailed in the Supporting Information.

2. THEORY

2.1. Preliminary Considerations. In what follows, we focus on applying the GQME formalism to systems with an overall Hamiltonian of the following form, which is commonly used for modeling photosynthetic and photovoltaic systems:

$$\hat{H} = \sum_{j=1}^{N_e} \hat{H}_j |j\rangle\langle j| + \sum_{\substack{j,k=1 \\ k\neq j}}^{N_e} \hat{V}_{jk} |j\rangle\langle k| \tag{1}$$

Here, $\hat{H}_j = \hat{\mathbf{P}}^2/2 + V_j(\hat{\mathbf{R}})$ is the nuclear Hamiltonian when the system is in the diabatic electronic state $|j\rangle$, with the index j running over the N_e electronic states, $\{\hat{V}_{jk} | j \neq k\}$ are coupling terms between electronic states, and $\hat{\mathbf{R}} = (\hat{R}_1, ..., \hat{R}_{N_n})$ and $\hat{\mathbf{P}} = (\hat{P}_1, ..., \hat{P}_{N_n})$ are the mass-weighted position and momentum operators of the $N_n \gg 1$ nuclear DOF. Throughout this article, boldfaced variables, for example, $\mathbf{A}$, indicate vector quantities, a hat over a variable, for example, $\hat{B}$, indicates an operator quantity, and script font, for example, $\mathcal{C}$, indicates a superoperator.

https://doi.org/10.1021/acs.jpcb.1c05719
J. Phys. Chem. B 2021, 125, 9834−9852

The initial state of the overall system is assumed to be of the following single product form:

$$\hat{\rho}(0) = \hat{\rho}_n(0) \otimes \hat{\sigma}(0) \tag{2}$$

Here, $\hat{\rho}_n(t) = \mathrm{Tr}_e\{\hat{\rho}(t)\}$ and $\hat{\sigma}(t) = \mathrm{Tr}_n\{\hat{\rho}(t)\}$ are the reduced density operators that describe the states of the nuclear DOF and electronic DOF, respectively, and $\mathrm{Tr}_e\{...\}$ and $\mathrm{Tr}_n\{...\}$ stand for partially tracing over the electronic Hilbert space and the nuclear Hilbert space, respectively.

The overall system state at a later time t is given by the density operator

$$\begin{aligned}\hat{\rho}(t) &= e^{-i\hat{H}t/\hbar}\,\hat{\rho}_n(0) \otimes \hat{\sigma}(0)\, e^{i\hat{H}t/\hbar} \\ &\equiv e^{-i\mathcal{L}t/\hbar}\,\hat{\rho}_n(0) \otimes \hat{\sigma}(0)\end{aligned} \tag{3}$$

where $\hat{H}$ is the overall Hamiltonian given in eq 1 and $\mathcal{L}(\cdot) = [\hat{H}, \cdot]$ is the corresponding Liouvillian superoperator. The reduced electronic density operator at time t is given by

$$\hat{\sigma}(t) = \mathrm{Tr}_n\{\hat{\rho}(t)\} = \sum_{j,k=1}^{N_e} \sigma_{jk}(t)|j\rangle\langle k| \tag{4}$$

The electronic populations and coherences are given by $\{\sigma_{jj}(t) = \langle j|\hat{\sigma}(t)|j\rangle\}$ and $\{\sigma_{jk}(t) = \langle j|\hat{\sigma}(t)|k\rangle | j \neq k\}$, respectively. Importantly, the time evolution of the electronic populations and coherences underlies energy, charge, and coherence transfer dynamics.

2.2. System-Bath GQME vs Modified GQME. In this article, we will compare and contrast two types of GQMEs, which differ with respect to the form of the overall Hamiltonian with which one starts out. One type is based on casting the overall Hamiltonian in eq 1 in a system-bath form, that is, as a sum of system, bath, and system-bath coupling terms, and therefore this type is denoted the *system-bath GQME*. Since the overall Hamiltonian of the form given in eq 1 can be cast in multiple different system-bath forms, another type of GQME was recently proposed that avoids recasting the overall Hamiltonian in a system-bath form. The type of GQME obtained this way has been denoted the *modified GQME*. Importantly, while the two types of GQMEs are expected to yield the same electronic dynamics when the memory kernel is obtained from quantum-mechanically exact projection-free inputs, this need not be and is often not the case when the projection-free inputs are obtained via approximate methods.

In the next two subsections, we will provide short summaries of these two types of GQMEs. For the system-bath GQME, the reader is referred to refs 22−24 for further details. For the modified GQME, the reader is referred to refs 38−40 for further details.

2.2.1. The System-Bath GQME. The derivation of the system-bath GQME starts out by casting the Hamiltonian in eq 1 in a system-bath form:

$$\hat{H} = \hat{H}_S + \hat{H}_B + \hat{H}_{BS} \tag{5}$$

Here, $\hat{H}_S$ is the system Hamiltonian, $\hat{H}_B$ is the bath Hamiltonian, and $\hat{H}_{BS}$ is the coupling between system and bath. For the type of systems under consideration here, the system would stand for the electronic DOF, the bath would stand for the nuclear DOF, and the system−bath coupling, $\hat{H}_{BS}$, would stand for the coupling between the nuclear and electronic DOF. However, it should be noted that these assignments do not dictate a unique system-bath form.[38] Finally, we note that each term on the r.h.s. of eq 5 has a matching Liouvillian operator, that is, $\mathcal{L} = \mathcal{L}_S + \mathcal{L}_B + \mathcal{L}_{BS}$, where $\mathcal{L}_S = [\hat{H}_S, \cdot]$, $\mathcal{L}_B = [\hat{H}_B, \cdot]$, and $\mathcal{L}_{BS} = [\hat{H}_{BS}, \cdot]$.

Within the system-bath GQME, the initial nuclear density operator [see eq 2] typically corresponds to thermal equilibrium with respect to the bath Hamiltonian:

$$\hat{\rho}_n(0) = \hat{\rho}_B^{eq} = \frac{e^{-\beta\hat{H}_B}}{\mathrm{Tr}_B\{e^{-\beta\hat{H}_B}\}} \tag{6}$$

Here, $\mathrm{Tr}_B\{...\}$ corresponds to tracing over the bath/nuclear DOF. It is also often assumed, without loss of generality, that $\hat{H}_{BS}$ is defined such that

$$\langle\hat{H}_{BS}\rangle_B^{eq} \equiv \mathrm{Tr}_B\{\hat{\rho}_B^{eq}\hat{H}_{BS}\} = 0 \tag{7}$$

Using a projection operator of the form

$$\mathcal{P}(\cdot) = \hat{\rho}_B^{eq} \otimes \mathrm{Tr}_B\{\cdot\} \tag{8}$$

the quantum-mechanically exact dynamics of the system reduced density operator can then be shown to be governed by the *system-bath GQME*, which has the following form:

$$\frac{d}{dt}\hat{\sigma}(t) = -\frac{i}{\hbar}\mathcal{L}_S\hat{\sigma}(t) - \int_0^t d\tau\, \mathcal{K}^{SB}(\tau)\hat{\sigma}(t-\tau) \tag{9}$$

Here, $-i\mathcal{L}_S\hat{\sigma}(t)/\hbar$ and $-\int_0^t d\tau\, \mathcal{K}^{SB}(\tau)\hat{\sigma}(t-\tau)$ correspond to the bath-free and bath-induced contributions to the system's reduced dynamics, respectively, and $\mathcal{K}^{SB}(\tau)$ is the memory kernel superoperator (the explicit form of the system-bath memory kernel will be given in section 2.3).

As discussed in ref 38, while the system-bath approach has been used successfully in the past, it is neither natural nor convenient for an overall Hamiltonian of the form given in eq 1. This is because it is impossible to come up with a uniquely defined bath Hamiltonian, $\hat{H}_B$, since the first term in eq 1, $\sum_j \hat{H}_j|j\rangle\langle j|$, associates a different nuclear Hamiltonian, $\hat{H}_j$, with each electronic state $|j\rangle$. This lack of a unique system-bath form can give rise to complications when using a GQME-based approach:

- Different choices of $\hat{H}_B$, $\hat{H}_S$, and $\hat{H}_{BS}$ can lead to different results when an approximate method is used to obtain the projection-free inputs needed for calculating $\mathcal{K}^{SB}(\tau)$, with no clear criterion for choosing between them.
- The assumption that the nuclear DOF start at equilibrium with respect to $\hat{H}_B$ [see eq 6] means that the definition of $\hat{H}_B$ needs to change whenever the nuclear initial state does.
- Since the system-bath coupling, $\hat{H}_{BS}$, is often defined as in eq 7 and the projection operator, $\mathcal{P}$, is as defined in eq 8, the definition of $\hat{H}_{BS}$ and $\mathcal{P}$ also depend on the choice of $\hat{H}_B$.
- The second term in eq 1, $\sum_{j,k\neq j}\hat{V}_{jk}|j\rangle\langle k|$, becomes purely electronic within the Condon approximation, $\hat{V}_{jk} \rightarrow V_{jk}$, and would be part of the system Hamiltonian, $\hat{H}_S$. However, in the non-Condon case, it is part of the system-bath coupling term, $\hat{H}_{BS}$, making it difficult to create a unified framework for Condon and non-Condon cases.

https://doi.org/10.1021/acs.jpcb.1c05719
J. Phys. Chem. B 2021, 125, 9834−9852

2.2.2. The Modified GQME. In contrast to the system-bath GQME, the modified GQME starts out by casting the overall Hamiltonian in eq 1 as a sum of two terms, $\hat{H} = \hat{H}_{zero} + \hat{H}_{int}$, where the zero Hamiltonian, $\hat{H}_{zero}$, and the interaction Hamiltonian, $\hat{H}_{int}$, are given by

$$\hat{H}_{zero} = \sum_{j=1}^{N_e} \hat{H}_j|j\rangle\langle j|, \quad \hat{H}_{int} = \sum_{\substack{j,k=1 \\ k\neq j}}^{N_e} \hat{V}_{jk}|j\rangle\langle k| \tag{10}$$

Each term has a matching Liouvillian operator, given by $\mathcal{L}_{zero}(\cdot) = [\hat{H}_{zero}, \cdot]$ and $\mathcal{L}_{int}(\cdot) = [\hat{H}_{int}, \cdot]$. In the Condon approximation, the electronic coupling terms are constants, $\hat{V}_{jk} \to V_{jk}$, making $\hat{H}_{int}$ a purely electronic operator and $\mathcal{L}_{int}$ a purely electronic superoperator.

Defining the projection operator as

$$\mathcal{P}(\cdot) = \hat{\rho}_n(0) \otimes \mathrm{Tr}_n\{\cdot\} \tag{11}$$

leads to the following *modified GQME* for the electronic reduced density operator, $\hat{\sigma}(t)$:

$$\frac{\mathrm{d}}{\mathrm{d}t}\hat{\sigma}(t) = -\frac{i}{\hbar}\langle\mathcal{L}\rangle_n^0\hat{\sigma}(t) - \int_0^t \mathrm{d}\tau\, \mathcal{K}^M(\tau)\hat{\sigma}(t-\tau) \tag{12}$$

Here, $\mathcal{K}^M(\tau)$ is the modified memory kernel superoperator [which is not the same as $\mathcal{K}^{SB}(\tau)$ and whose explicit form will be given in section 2.3] and $\langle\mathcal{L}\rangle_n^0$ is the overall Liouvillian averaged over the initial state of the nuclear DOF, resulting in a purely electronic superoperator, which is given by

$$\begin{aligned}\langle\mathcal{L}\rangle_n^0(\cdot) &\equiv \mathrm{Tr}_n\{\hat{\rho}_n(0)\mathcal{L}\}(\cdot) \\ &= \sum_{j=1}^{N_e}\langle\hat{H}_j\rangle_n^0[|j\rangle\langle j|, \cdot] + \sum_{\substack{j,k=1 \\ k\neq j}}^{N_e}\langle\hat{V}_{jk}\rangle_n^0[|j\rangle\langle k|, \cdot]\end{aligned} \tag{13}$$

It should be noted that the modified GQME does not suffer from the aforementioned ambiguities that the system-bath GQME suffers from.

2.3. Representations of the Memory Kernel. In this section, we outline eight different possible representations of the memory kernel. The eight representations can be grouped based on the GQME to which they correspond, the system-bath GQME, eq 9, or the modified GQME, eq 12.

Starting with the system-bath GQME, we will compare and contrast the following four representations of the memory kernel:[22,24,38]

$$\mathcal{K}^{SB}(\tau) = \frac{1}{\hbar^2}\mathrm{Tr}_B\{\mathcal{L}_{BS}\, e^{-i(\mathcal{L}-\mathcal{L}_{BS}\mathcal{P})\tau/\hbar}\mathcal{L}_{BS}\hat{\rho}_B^{eq}\} \tag{14}$$

$$\mathcal{K}^{SB}(\tau) = \frac{1}{\hbar^2}\mathrm{Tr}_B\{\mathcal{L}_{BS}\, e^{-i\mathcal{Q}\mathcal{L}\tau/\hbar}\mathcal{Q}\mathcal{L}\hat{\rho}_B^{eq}\} \tag{15}$$

$$\mathcal{K}^{SB}(\tau) = \frac{1}{\hbar^2}\mathrm{Tr}_B\{\mathcal{L}_{BS}\, e^{-i\mathcal{Q}\mathcal{L}\tau/\hbar}\mathcal{Q}\mathcal{L}_{BS}\hat{\rho}_B^{eq}\} \tag{16}$$

$$\mathcal{K}^{SB}(\tau) = \frac{1}{\hbar^2}\mathrm{Tr}_B\{\mathcal{L}_{BS}\mathcal{Q}e^{-i\mathcal{L}\mathcal{Q}\tau/\hbar}\mathcal{L}_{BS}\hat{\rho}_B^{eq}\} \tag{17}$$

where $\mathcal{Q} = \mathcal{I} - \mathcal{P}$ and $\mathcal{I}$ is the unity superoperator. It should be noted that while these correspond to different representations of the same memory kernel when calculated via quantum-mechanically exact methods, they can and do yield different results when approximate methods are used.

Starting with the modified GQME, we will also compare and contrast four representations of the memory kernel. The first two representations avoid the Condon approximation and are given by

$$\mathcal{K}^M(\tau) = \frac{1}{\hbar^2}\mathrm{Tr}_n\{\mathcal{L}\, e^{-i\mathcal{Q}\mathcal{L}\tau/\hbar}\mathcal{Q}\mathcal{L}\hat{\rho}_n(0)\} \tag{18}$$

$$\mathcal{K}^M(\tau) = \frac{1}{\hbar^2}\mathrm{Tr}_n\{\mathcal{L}\mathcal{Q}e^{-i\mathcal{L}\mathcal{Q}\tau/\hbar}\mathcal{L}\hat{\rho}_n(0)\} \tag{19}$$

The remaining two representations are only valid when the Condon approximation is valid and are given by

$$\mathcal{K}^M(\tau) = \frac{1}{\hbar^2}\mathrm{Tr}_n\{\mathcal{L}_{zero}\, e^{-i\mathcal{Q}L\tau/\hbar}\mathcal{Q}L_{zero}\hat{\rho}_n(0)\} \tag{20}$$

$$\mathcal{K}^M(\tau) = \frac{1}{\hbar^2}\mathrm{Tr}_n\{\mathcal{L}_{zero}\mathcal{Q}\, e^{-i\mathcal{L}\mathcal{Q}\tau/\hbar}\mathcal{L}_{zero}\hat{\rho}_n(0)\} \tag{21}$$

More details and derivations of these memory kernels can be found in refs 22, 24, 33, and 38.

It should be noted that $\mathcal{L}_{BS}$ is usually not equivalent to $\mathcal{L}_{zero}$ and so, despite similar forms between eqs 16 and 20 and between eqs 17 and 21, these are different memory kernels that can result in different results when approximate methods are used.

2.4. Approaches for Obtaining the Memory Kernel. In this section, we outline ten different approaches for obtaining the memory kernel. These approaches can be grouped based on whether they obtain the memory kernel of the system-bath or modified GQME. This distinction will be denoted by including either *System-Bath* and *SB* or *Modified* and *M* in the name and abbreviation, respectively, that we use for the approach.

The approaches for obtaining the memory kernel can be further distinguished based on whether one needs one or two integral equations to obtain the memory kernel from projection-free inputs. Three approaches, one for the system-bath GQME and two for the modified GQME, require solving two integral equations to obtain the memory kernel. The first equation is a Volterra integral equation of the second type to obtain an auxiliary projection-dependent input for the second equation, which yields the memory kernel from the projection-free and projection-dependent inputs. These three approaches are designated by including *Two-Equation* and *TE* in their titles and abbreviations, respectively.

All of the remaining seven approaches require solving a single Volterra equation to obtain the memory kernel from the projection-free inputs. These seven approaches can be further distinguished based on the order in which the projection superoperator, $\mathcal{Q}$, and the overall Liouvillian superoperator, $\mathcal{L}$, appear in the power of the exponential operator within the memory kernel. More specifically, $\mathcal{Q}$ precedes $\mathcal{L}$ for the memory kernel representations in eqs 15, 16, 18, and 20, while in contrast, $\mathcal{L}$ precedes $\mathcal{Q}$ for the memory kernel representations in eqs 17, 19, and 21. In light of this, we denote the four approaches that use the representation of the memory kernel in eqs 15, 16, 18, and 20 as *Projection-First (PF)* and the three approaches that use the representation of the memory kernel in eqs 17, 19, and 21 as *Projection-Second (PS)*.

https://doi.org/10.1021/acs.jpcb.1c05719
J. Phys. Chem. B 2021, 125, 9834−9852

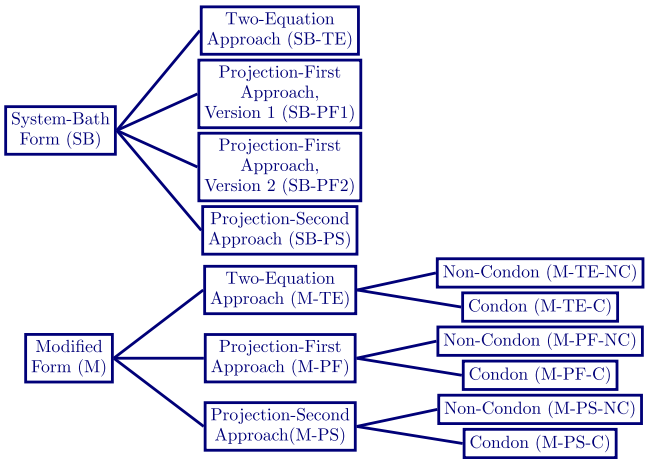

Figure 1. Tree diagram of the ten approaches to obtaining the memory kernel of the GQME under consideration in this article.

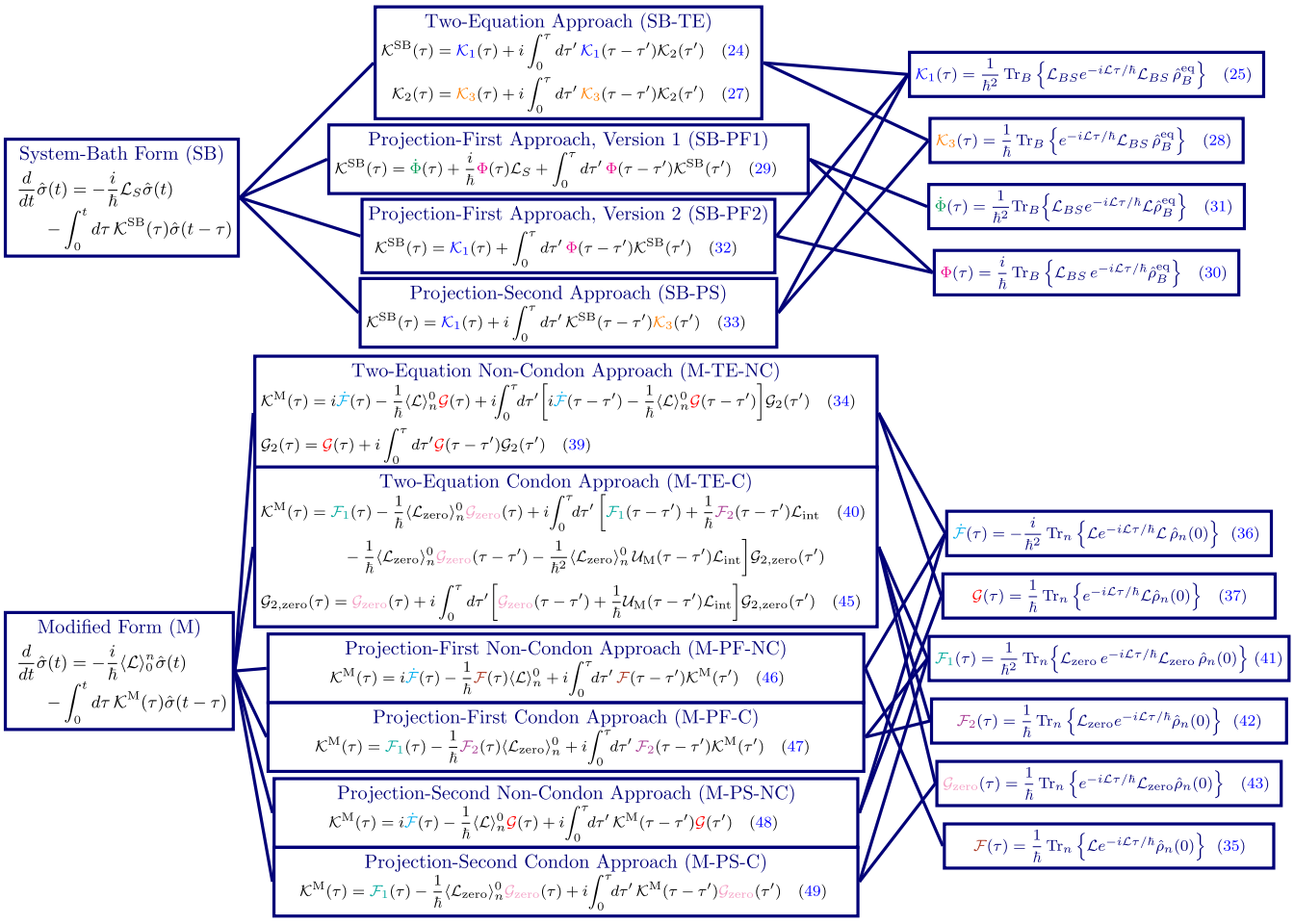

Figure 2. Tree diagram of the ten approaches to obtaining the memory kernel of the GQME under consideration in this article, including equations.

The system-bath GQME gives rise to four different system-bath approaches: one two-equation approach, two projection-first approaches, and one projection-second approach. The modified GQME gives rise to three different ways for calculating the memory kernel, each of which has a non-Condon and a Condon version, thereby leading to a total of six different approaches. Combined with the four approaches that are based on the system-bath GQME, there are ten different approaches for obtaining the memory kernel. The list of titles and abbreviations of these approaches is given as

- system-bath two-equation (SB-TE)
- system-bath projection-first, version 1 (SB-PF1)
- system-bath projection-first, version 2 (SB-PF2)
- system-bath projection-second (SB-PS)
- modified two-equation non-Condon (M-TE-NC)
- modified two-equation Condon (M-TE-C)

https://doi.org/10.1021/acs.jpcb.1c05719
J. Phys. Chem. B 2021, 125, 9834−9852

- modified projection-first non-Condon (M-PF-NC)
- modified projection-first Condon (M-PF-C)
- modified projection-second non-Condon (M-PS-NC)
- modified projection-second Condon (M-PS-C)

and can be visualized using the titles-only tree diagram shown in Figure 1. These ten approaches are further detailed in the following subsections, with a more detailed tree diagram given in Figure 2. The major aspects of and differences between the approaches are also summarized in 1.

Table 1. Comparison of Approaches[a]

Approach	Number of Equations	Projection-Free Inputs	Static or Dynamic Nuclear Operator(s)
SB-TE	Two	$\mathcal{K}_1(\tau)$	Both
		$\mathcal{K}_3(\tau)$	Static
SB-PF1	One	$\dot{\Phi}(\tau)$	Both
		$\Phi(\tau)$	Dynamic
SB-PF2	One	$\mathcal{K}_1(\tau)$	Both
		$\Phi(\tau)$	Dynamic
SB-PS	One	$\mathcal{K}_1(\tau)$	Both
		$\mathcal{K}_3(\tau)$	Static
M-TE-NC	Two	$\dot{\mathcal{F}}(\tau)$	Both
		$\mathcal{G}(\tau)$	Static
M-TE-C	Two	$\mathcal{F}_1(\tau)$	Both
		$\mathcal{F}_2(\tau)$	Dynamic
		$\mathcal{G}_{\text{zero}}(\tau)$	Static
M-PF-NC	One	$\dot{\mathcal{F}}(\tau)$	Both
		$\mathcal{F}(\tau)$	Dynamic
M-PF-C	One	$\mathcal{F}_1(\tau)$	Both
		$\mathcal{F}_2(\tau)$	Dynamic
M-PS-NC	One	$\dot{\mathcal{F}}(\tau)$	Both
		$\mathcal{G}(\tau)$	Static
M-PS-C	One	$\mathcal{F}_1(\tau)$	Both
		$\mathcal{G}_{\text{zero}}(\tau)$	Static

[a]This table summarizes important aspects of the approaches for obtaining the memory kernel of the GQME. Indicated in the second column are the number of integral equations necessary to obtain the memory kernel. The third column gives the projection-free inputs involved in the calculation of the memory kernel, color-coded to assist the identification of which approaches share projection-free inputs. The last column indicates whether the nuclear operators in the projection-free input are all static, all dynamic, or both (see section 2.5).

In the following subsections, we describe these ten different approaches for obtaining the memory kernel of the system-bath and modified GQMEs from projection-free inputs. In all cases, the relationships between the memory kernel and the projection-free inputs can be derived based on one of the following two identities:[22,24,41,42]

$$e^{-i\mathcal{B}\tau/\hbar} = e^{-i\mathcal{A}\tau/\hbar} - \frac{i}{\hbar}\int_0^\tau d\tau'\, e^{-i\mathcal{A}(\tau-\tau')/\hbar}(\mathcal{B}-\mathcal{A})\, e^{-i\mathcal{B}\tau'/\hbar} \tag{22}$$

$$e^{-i\mathcal{B}\tau/\hbar} = e^{-i\mathcal{A}\tau/\hbar} - \frac{i}{\hbar}\int_0^\tau d\tau'\, e^{-i\mathcal{A}\tau'/\hbar}(\mathcal{B}-\mathcal{A})\, e^{-i\mathcal{B}(\tau-\tau')/\hbar} \tag{23}$$

2.4.1. System-Bath Two-Equation Approach (SB-TE). The system-bath two-equation approach (SB-TE) for calculating the memory kernel is the same as the original Shi−Geva approach introduced in ref 22 and also used in refs 23, 38, and 40. It is based on the expression for the memory kernel of the form given in eq 14. Substituting $\mathcal{A}=\mathcal{L}$ and $\mathcal{B}=\mathcal{L}-\mathcal{L}_{\text{BS}}\mathcal{P}$ into the operator identity in eq 22 and plugging that into the memory kernel in eq 14 gives the following expression for the memory kernel

$$\mathcal{K}^{\text{SB}}(\tau) = \mathcal{K}_1(\tau) + i\int_0^\tau \mathcal{K}_1(\tau-\tau')\mathcal{K}_2(\tau') \tag{24}$$

where

$$\mathcal{K}_1(\tau) = \frac{1}{\hbar^2}\,\text{Tr}_{\text{B}}\{\mathcal{L}_{\text{BS}}\, e^{-i\mathcal{L}\tau/\hbar}\,\mathcal{L}_{\text{BS}}\hat{\rho}_{\text{B}}^{\text{eq}}\} \tag{25}$$

$$\mathcal{K}_2(\tau) = \frac{1}{\hbar}\,\text{Tr}_{\text{B}}\{e^{-i(\mathcal{L}-\mathcal{L}_{\text{BS}}\mathcal{P})\tau/\hbar}\,\mathcal{L}_{\text{BS}}\hat{\rho}_{\text{B}}^{\text{eq}}\} \tag{26}$$

Repeating the process for $\mathcal{K}_2(\tau)$, since it is projection-dependent, leads to the Volterra equation

$$\mathcal{K}_2(\tau) = \mathcal{K}_3(\tau) + i\int_0^\tau d\tau'\,\mathcal{K}_3(\tau-\tau')\mathcal{K}_2(\tau') \tag{27}$$

where

$$\mathcal{K}_3(\tau) = \frac{1}{\hbar}\,\text{Tr}_{\text{B}}\{e^{-i\mathcal{L}\tau/\hbar}\mathcal{L}_{\text{BS}}\hat{\rho}_{\text{B}}^{\text{eq}}\} \tag{28}$$

Thus, obtaining the memory kernel via the SB-TE approach requires first calculating the projection-free $\mathcal{K}_1(\tau)$ and $\mathcal{K}_3(\tau)$, then calculating $\mathcal{K}_2(\tau)$ through eq 27, and finally calculating $\mathcal{K}^{\text{SB}}(\tau)$ via eq 24.

2.4.2. System-Bath Projection-First Approach, Version 1 (SB-PF1). The system-bath projection-first approach, version 1 (SB-PF1), is the same as the Zhang−Ka−Geva approach introduced in ref 24 and also used in ref 38. It is based on the expression for the memory kernel of the form given in eq 15. Substituting $\mathcal{A}=\mathcal{L}$ and $\mathcal{B}=\mathcal{Q}\mathcal{L}$ into eq 22 and plugging that into the memory kernel in eq 15 leads to the following Volterra equation for $\mathcal{K}^{\text{SB}}(\tau)$:

$$\mathcal{K}^{\text{SB}}(\tau) = \dot{\Phi}(\tau) + \frac{i}{\hbar}\Phi(\tau)\mathcal{L}_{\text{S}} + \int_0^\tau d\tau'\Phi(\tau-\tau')\mathcal{K}^{\text{SB}}(\tau') \tag{29}$$

where $\Phi(\tau)$ and $\dot{\Phi}(\tau)$ are the projection-free inputs

$$\Phi(\tau) = \frac{i}{\hbar}\,\text{Tr}_{\text{B}}\{\mathcal{L}_{\text{BS}}\, e^{-i\mathcal{L}\tau/\hbar}\,\hat{\rho}_{\text{B}}^{\text{eq}}\} \tag{30}$$

$$\dot{\Phi}(\tau) = \frac{1}{\hbar^2}\,\text{Tr}_{\text{B}}\{\mathcal{L}_{\text{BS}}\, e^{-i\mathcal{L}\tau/\hbar}\,\mathcal{L}\hat{\rho}_{\text{B}}^{\text{eq}}\} \tag{31}$$

It should be noted that although $\dot{\Phi}(\tau)$ is the time derivative of $\Phi(\tau)$, it is meant to be calculated explicitly (when calculated via approximate methods), rather than obtained by calculating the time derivative of $\Phi(\tau)$ numerically.

Thus, obtaining the memory kernel via the SB-PF1 approach requires first calculating the projection-free $\Phi(\tau)$ and $\dot{\Phi}(\tau)$ and then calculating the memory kernel via eq 29.

2.4.3. System-Bath Projection-First Approach, Version 2 (SB-PF2). The system-bath projection-first approach, version 2 (SB-PF2), was previously introduced by Montoya-Castillo and Reichman in ref 33. It is based on the expression for the memory kernel of the form given in eq 16. Substituting

https://doi.org/10.1021/acs.jpcb.1c05719
J. Phys. Chem. B 2021, 125, 9834−9852

$\mathcal{A} = \mathcal{L}$ and $\mathcal{B} = \mathcal{QL}$ into eq 22 and plugging that into eq 16 leads to a Volterra equation of the form

$$\mathcal{K}^{\mathrm{SB}}(\tau) = \mathcal{K}_1(\tau) + \int_0^\tau \mathrm{d}\tau'\, \Phi(\tau - \tau')\mathcal{K}^{\mathrm{SB}}(\tau') \tag{32}$$

where $\mathcal{K}_1(\tau)$ is given in eq 25 and $\Phi(\tau)$ is given in eq 30.

Thus, obtaining the memory kernel via the SB-PF2 approach requires first calculating projection-free $\mathcal{K}_1(\tau)$ and $\Phi(\tau)$ and then calculating the memory kernel from them based on eq 32. Notably, this approach uses a combination of projection-free inputs that are also used in the SB-TE [$\mathcal{K}_1(\tau)$] and SB-PF1 [$\Phi(\tau)$] approaches. However, the way the memory kernel is obtained from these projection-free inputs is based on a different Volterra equation [eq 32] than that used in the SB-TE and SB-PF1 approaches.

2.4.4. System-Bath Projection-Second Approach (SB-PS). The system-bath projection-second approach (SB-PS) was also previously introduced by Montoya-Castillo and Reichman in ref 33 and also used in ref 37. It is based on the expression for the memory kernel of the form given in eq 17. Substituting $\mathcal{A} = \mathcal{LQ}$ and $\mathcal{B} = \mathcal{L}$ into eq 23 and plugging that into eq 17 leads to a Volterra equation of the form

$$\mathcal{K}^{\mathrm{SB}}(\tau) = \mathcal{K}_1(\tau) + i\int_0^\tau \mathrm{d}\tau'\, \mathcal{K}^{\mathrm{SB}}(\tau - \tau')\mathcal{K}_3(\tau') \tag{33}$$

where $\mathcal{K}_1(\tau)$ is given in eq 25 and $\mathcal{K}_3(\tau)$ is given in eq 28.

Thus, obtaining the memory kernel via the SB-PS approach requires first calculating the projection-free $\mathcal{K}_1(\tau)$ and $\mathcal{K}_3(\tau)$ and then calculating the memory kernel via eq 33. Notably, this approach uses the same projection-free inputs as the SB-TE approach [$\mathcal{K}_1(\tau)$ and $\mathcal{K}_3(\tau)$]. However, the way the memory kernel is obtained from these projection-free inputs is based on a single Volterra equation rather than on two coupled equations.

2.4.5. Modified Two-Equation Non-Condon Approach (M-TE-NC). The modified two-equation non-Condon approach (M-TE-NC) is based on the expression for the memory kernel of the form given in eq 19. Substituting $\mathcal{A} = \mathcal{L}$ and $\mathcal{B} = \mathcal{LQ}$ into the operator identity in eq 22 and plugging into eq 19 gives the following expressions for the memory kernel

$$\begin{aligned}\mathcal{K}^{\mathrm{M}}(\tau) = {} & i\dot{\mathcal{F}}(\tau) - \frac{1}{\hbar}\langle\mathcal{L}\rangle_{\mathrm{n}}^{0}\mathcal{G}(\tau) \\ & + i\int_0^\tau \mathrm{d}\tau' \left[i\dot{\mathcal{F}}(\tau - \tau') - \frac{1}{\hbar}\langle\mathcal{L}\rangle_{\mathrm{n}}^{0}\mathcal{G}(\tau - \tau')\right]\mathcal{G}_2(\tau')\end{aligned} \tag{34}$$

Here, $\dot{\mathcal{F}}(\tau)$ is the time-derivative of $\mathcal{F}(\tau)$ and both are given by

$$\mathcal{F}(\tau) = \frac{1}{\hbar}\,\mathrm{Tr}_{\mathrm{n}}\{\mathcal{L}\,\mathrm{e}^{-i\mathcal{L}\tau/\hbar}\,\hat{\rho}_{\mathrm{n}}(0)\} \tag{35}$$

$$\dot{\mathcal{F}}(\tau) = -\frac{i}{\hbar^2}\,\mathrm{Tr}_{\mathrm{n}}\{\mathcal{L}\,\mathrm{e}^{-i\mathcal{L}\tau/\hbar}\,\mathcal{L}\hat{\rho}_{\mathrm{n}}(0)\} \tag{36}$$

It should be noted that although $\dot{\mathcal{F}}(\tau)$ is the time derivative of $\mathcal{F}(\tau)$, it is meant to be calculated explicitly (when calculated via approximate methods), rather than obtained by calculating the time derivative of $\mathcal{F}(\tau)$ numerically. $\mathcal{G}(\tau)$ and $\mathcal{G}_2(\tau)$ are given by

$$\mathcal{G}(\tau) = \frac{1}{\hbar}\,\mathrm{Tr}_{\mathrm{n}}\{\mathrm{e}^{-i\mathcal{L}\tau/\hbar}\,\mathcal{L}\hat{\rho}_{\mathrm{n}}(0)\} \tag{37}$$

$$\mathcal{G}_2(\tau) = \frac{1}{\hbar}\,\mathrm{Tr}_{\mathrm{n}}\{\mathrm{e}^{-i\mathcal{LQ}\tau/\hbar}\,\mathcal{L}\hat{\rho}_{\mathrm{n}}(0)\} \tag{38}$$

Since $\mathcal{G}_2(\tau)$ is projection-dependent, we need to repeat the process to obtain a Volterra equation for $\mathcal{G}_2(\tau)$. Substituting $\mathcal{A} = \mathcal{L}$ and $\mathcal{B} = \mathcal{LQ}$ into the operator identity in eq 22 and plugging into eq 38 leads to the following Volterra equation for $\mathcal{G}_2(\tau)$:

$$\mathcal{G}_2(\tau) = \mathcal{G}(\tau) + i\int_0^\tau \mathrm{d}\tau'\, \mathcal{G}(\tau - \tau')\mathcal{G}_2(\tau') \tag{39}$$

Thus, obtaining the memory kernel via the M-TE-NC approach requires first calculating the projection-free $\dot{\mathcal{F}}(\tau)$ and $\mathcal{G}(\tau)$, then calculating $\mathcal{G}_2(\tau)$ through eq 39, and finally calculating $\mathcal{K}^{\mathrm{M}}(\tau)$ via eq 34.

2.4.6. Modified Two-Equation Condon Approach (M-TE-C). The modified two-equation Condon approach (M-TE-C) starts from a memory kernel of the form given in eq 21. Substituting $\mathcal{A} = \mathcal{L}$ and $\mathcal{B} = \mathcal{LQ}$ into the operator identity in eq 22 and plugging into eq 21 leads to the following Volterra equation

$$\begin{aligned}\mathcal{K}^{\mathrm{M}}(\tau) = {} & \mathcal{F}_1(\tau) - \frac{1}{\hbar}\langle\mathcal{L}_{\mathrm{zero}}\rangle_{\mathrm{n}}^{0}\mathcal{G}_{\mathrm{zero}}(\tau) \\ & + i\int_0^\tau \mathrm{d}\tau' \left[\mathcal{F}_1(\tau - \tau') + \frac{1}{\hbar}\mathcal{F}_2(\tau - \tau')\mathcal{L}_{\mathrm{int}}\right. \\ & - \frac{1}{\hbar}\langle\mathcal{L}_{\mathrm{zero}}\rangle_{\mathrm{n}}^{0}\mathcal{G}_{\mathrm{zero}}(\tau - \tau') \\ & \left. - \frac{1}{\hbar^2}\langle\mathcal{L}_{\mathrm{zero}}\rangle_{\mathrm{n}}^{0}\mathcal{U}_{\mathrm{M}}(\tau - \tau')\mathcal{L}_{\mathrm{int}}\right]\mathcal{G}_{2,\mathrm{zero}}(\tau')\end{aligned} \tag{40}$$

with the derivation of eq 40 given in the Supporting Information. $\mathcal{F}_1(\tau)$, $\mathcal{F}_2(\tau)$, $\mathcal{G}_{\mathrm{zero}}(\tau)$, and $\mathcal{G}_{2,\mathrm{zero}}(\tau)$ are given by

$$\mathcal{F}_1(\tau) = \frac{1}{\hbar^2}\,\mathrm{Tr}_{n}\{\mathcal{L}_{\mathrm{zero}}\,\mathrm{e}^{-i\mathcal{L}\tau/\hbar}\,\mathcal{L}_{\mathrm{zero}}\,\hat{\rho}_{\mathrm{n}}(0)\} \tag{41}$$

$$\mathcal{F}_2(\tau) = \frac{1}{\hbar}\,\mathrm{Tr}_{\mathrm{n}}\{\mathcal{L}_{\mathrm{zero}}\,\mathrm{e}^{-i\mathcal{L}\tau/\hbar}\,\hat{\rho}_{\mathrm{n}}(0)\} \tag{42}$$

$$\mathcal{G}_{\mathrm{zero}}(\tau) = \frac{1}{\hbar}\,\mathrm{Tr}_{\mathrm{n}}\{\mathrm{e}^{-i\mathcal{L}\tau/\hbar}\,\mathcal{L}_{\mathrm{zero}}\,\hat{\rho}_{\mathrm{n}}(0)\} \tag{43}$$

$$\mathcal{G}_{2,\mathrm{zero}}(\tau) = \frac{1}{\hbar}\,\mathrm{Tr}_{\mathrm{n}}\{\mathrm{e}^{-i\mathcal{LQ}\tau/\hbar}\,\mathcal{L}_{\mathrm{zero}}\,\hat{\rho}_{\mathrm{n}}(0)\} \tag{44}$$

Since $\mathcal{G}_{2,\mathrm{zero}}(\tau)$ is projection-dependent, we need to repeat the process to obtain a Volterra equation for $\mathcal{G}_{2,\mathrm{zero}}(\tau)$. Substituting $\mathcal{A} = \mathcal{L}$ and $\mathcal{B} = \mathcal{LQ}$ into the operator identity in eq 22 and plugging into eq 44 leads to the Volterra equation for $\mathcal{G}_{2,\mathrm{zero}}(\tau)$:

$$\begin{aligned}\mathcal{G}_{2,\mathrm{zero}}(\tau) = {} & \mathcal{G}_{\mathrm{zero}}(\tau) + i\int_0^\tau \mathrm{d}\tau' \left[\mathcal{G}_{\mathrm{zero}}(\tau - \tau')\right. \\ & \left. + \frac{1}{\hbar}\mathcal{U}_{\mathrm{M}}(\tau - \tau')\mathcal{L}_{\mathrm{int}}\right]\mathcal{G}_{2,\mathrm{zero}}(\tau')\end{aligned} \tag{45}$$

with $\mathcal{U}_{\mathrm{M}}(\tau) = \mathrm{Tr}_{\mathrm{n}}\{\mathrm{e}^{-i\mathcal{L}\tau/\hbar}\,\hat{\rho}_{n}(0)\}$ and the details of the derivation given in the Supporting Information.

https://doi.org/10.1021/acs.jpcb.1c05719
J. Phys. Chem. B 2021, 125, 9834−9852

Thus, obtaining the memory kernel via the M-TE-C approach requires first calculating the projection-free $\mathcal{F}_1(\tau)$, $\mathcal{F}_2(\tau)$, and $\mathcal{G}_{\text{zero}}(\tau)$, then calculating $\mathcal{G}_{2,\text{zero}}(\tau)$ through eq 45, and finally calculating $\mathcal{K}^{\text{M}}(\tau)$ via eq 40.

2.4.7. Modified Projection-First Non-Condon Approach (M-PF-NC). The modified projection-first non-Condon approach (M-PF-NC) is the same as the non-Condon modified approach introduced in ref 38 and described in refs 39 and 40. This approach uses a memory kernel of the form given in eq 18. Substituting $\mathcal{A} = \mathcal{L}$ and $\mathcal{B} = \mathcal{QL}$ into eq 22 and plugging the identity into eq 18 leads to the Volterra equation

$$\mathcal{K}^{\text{M}}(\tau) = i\dot{\mathcal{F}}(\tau) - \frac{1}{\hbar}\mathcal{F}(\tau)\langle\mathcal{L}\rangle_{\text{n}}^{0} + i\int_0^\tau \text{d}\tau'\mathcal{F}(\tau-\tau')\mathcal{K}^{\text{M}}(\tau') \tag{46}$$

where $\mathcal{F}(\tau)$ and $\dot{\mathcal{F}}(\tau)$ are given in eqs 35 and 36, respectively.

Thus, obtaining the memory kernel via the M-PF-NC approach requires first calculating the projection-free $\mathcal{F}(\tau)$ and $\dot{\mathcal{F}}(\tau)$ and then calculating $\mathcal{K}^{\text{M}}(\tau)$ via eq 46.

2.4.8. Modified Projection-First Condon Approach (M-PF-C). The modified projection-first Condon approach (M-PF-C) is the same as the Condon modified approach introduced in ref 38 and used in refs 39 and 40. This approach uses a memory kernel of the form given in eq 20. Substituting $\mathcal{A} = \mathcal{L}$ and $\mathcal{B} = \mathcal{QL}$ into eq 22 and plugging the identity into eq 20 leads to the Volterra equation

$$\mathcal{K}^{\text{M}}(\tau) = \mathcal{F}_1(\tau) - \frac{1}{\hbar}\mathcal{F}_2(\tau)\langle\mathcal{L}_{\text{zero}}\rangle_{\text{n}}^{0} + i\int_0^\tau \text{d}\tau'\,\mathcal{F}_2(\tau-\tau')\mathcal{K}^{\text{M}}(\tau') \tag{47}$$

where $\mathcal{F}_1(\tau)$ is given in eq 41 and $\mathcal{F}_2(\tau)$ is given in eq 42.

Thus, obtaining the memory kernel via the M-PF-C approach requires first calculating the projection-free $\mathcal{F}_1(\tau)$ and $\mathcal{F}_2(\tau)$ and then calculating $\mathcal{K}^{\text{M}}(\tau)$ via eq 47.

2.4.9. Modified Projection-Second Non-Condon Approach (M-PS-NC). The modified projection-second non-Condon approach (M-PS-NC) uses the same memory kernel as the M-TE-NC approach, eq 19. Substituting $\mathcal{A} = \mathcal{LQ}$ and $\mathcal{B} = \mathcal{L}$ into eq 22 and plugging the identity into eq 19 results in the Volterra equation

$$\mathcal{K}^{\text{M}}(\tau) = i\dot{\mathcal{F}}(\tau) - \frac{1}{\hbar}\langle\mathcal{L}\rangle_{\text{n}}^{0}\mathcal{G}(\tau) + i\int_0^\tau \text{d}\tau'\,\mathcal{K}^{\text{M}}(\tau-\tau')\mathcal{G}(\tau') \tag{48}$$

where $\dot{\mathcal{F}}(\tau)$ is given in eq 36 and $\mathcal{G}(\tau)$ is given in eq 37.

Thus, obtaining the memory kernel via the M-PS-NC approach requires first calculating the projection-free $\dot{\mathcal{F}}(\tau)$ and $\mathcal{G}(\tau)$ and then calculating $\mathcal{K}^{\text{M}}(\tau)$ via eq 48.

2.4.10. Modified Projection-Second Condon Approach (M-PS-C). The modified projection-second Condon approach (M-PS-C) uses the same memory kernel as the M-TE-C approach, eq 21. Substituting $\mathcal{A} = \mathcal{LQ}$ and $\mathcal{B} = \mathcal{L}$ into eq 22 and plugging the identity into eq 21 results in the Volterra equation

$$\mathcal{K}^{\text{M}}(\tau) = \mathcal{F}_1(\tau) - \frac{1}{\hbar}\langle\mathcal{L}_{\text{zero}}\rangle_{\text{n}}^{0}\mathcal{G}_{\text{zero}}(\tau) + i\int_0^\tau \text{d}\tau'\mathcal{K}^{\text{M}}(\tau-\tau')\mathcal{G}_{\text{zero}}(\tau') \tag{49}$$

where $\mathcal{F}_1(\tau)$ is given in eq 41 and $\mathcal{G}_{\text{zero}}(\tau)$ is given in eq 43.

Thus, obtaining the memory kernel via the M-PS-C approach requires first calculating the projection-free $\mathcal{F}_1(\tau)$ and $\mathcal{G}_{\text{zero}}(\tau)$ and then calculating $\mathcal{K}^{\text{M}}(\tau)$ via eq 49.

2.5. The Bare, Static, and Dynamic Forms of the Projection-Free Inputs. In this section, we consider three different forms of the projection-free inputs, which we will refer to below as *bare*, *static*, and *dynamic*. These forms were first introduced by Montoya-Castillo and Reichman in ref 33 (though they referred to them as expansions rather than forms), where they derived and tested them for the projection-free inputs of the SB-PF2 and SB-PS approaches. In what follows, we will derive and test these three forms for all the projection-free inputs needed for the ten approaches under consideration in this article.

We will demonstrate the derivation of the bare, static, and dynamic forms in the case of the projection-free input $\mathcal{F}_1(\tau)$. To this end, we will refer to the definition of $\mathcal{F}_1(\tau)$ as given in eq 41 as its *bare* form. When using this definition, the matrix elements of $\mathcal{F}_1(\tau)$ in terms of the diabatic electronic basis $\{|j\rangle;\ j = 1, \ldots, N_{\text{e}}\}$, are given by (here, a, b, c, d correspond to indices of the electronic states in tetradic notation):

$$\begin{aligned}\mathcal{F}_{1,abcd}(\tau) &= \text{Tr}_{\text{e}}\{(|a\rangle\langle b|)^{\dagger}\mathcal{F}_1(\tau)|c\rangle\langle d|\} \\ &= \frac{1}{\hbar^2}\text{Tr}\{(\hat{H}_c\,\hat{\rho}_{\text{n}}(0) - \hat{\rho}_{\text{n}}(0)\hat{H}_d)|c\rangle\langle d| \\ &\quad \times \text{e}^{i\hat{H}\tau/\hbar}(\hat{H}_a - \hat{H}_b)|b\rangle\langle a|\,\text{e}^{-i\hat{H}\tau/\hbar}\}\end{aligned} \tag{50}$$

Thus, the matrix elements of $\mathcal{F}_1(\tau)$ in the bare form are given by correlation functions (CFs) of the form $\text{Tr}\{\hat{A}\hat{B}(\tau)\}$, where $\hat{A}$ is a *static* operator, because it does not evolve in time while $\hat{B}(\tau) = \text{e}^{i\hat{H}\tau/\hbar}\hat{B}\,\text{e}^{-i\hat{H}\tau/\hbar}$ is a *dynamic* operator, because it does evolve in time. Importantly, the bare form gives rise to CFs where the $\hat{H}_c$ and $\hat{H}_d$ nuclear operators are *static*, while the $\hat{H}_a$ and $\hat{H}_b$ nuclear operators are *dynamic*. Thus, the bare form involves both static and dynamic nuclear operators for $\mathcal{F}_1(\tau)$.

In contrast to the bare form, the static and dynamic forms of $\mathcal{F}_1(\tau)$ are designed to be given in terms of CFs where the nuclear operators [other than $\hat{\rho}_{\text{n}}(0)$] are either all static or all dynamic, respectively. To obtain the *static* form of $\mathcal{F}_1(\tau)$, we start out by considering the time derivative of $i\mathcal{G}_{\text{zero}}(\tau)$ [see eq 43]:

$$\begin{aligned}i\frac{\text{d}}{\text{d}\tau}\mathcal{G}_{\text{zero}}(\tau) &= \frac{i}{\hbar}\frac{\text{d}}{\text{d}\tau}\text{Tr}_{\text{n}}\{\text{e}^{-i\mathcal{L}\tau/\hbar}\,\mathcal{L}_{\text{zero}}\,\hat{\rho}_{\text{n}}(0)\} \\ &= \frac{1}{\hbar^2}\text{Tr}_{\text{n}}\{\mathcal{L}\,\text{e}^{-i\mathcal{L}\tau/\hbar}\,\mathcal{L}_{\text{zero}}\,\hat{\rho}_{\text{n}}(0)\} \\ &= \frac{1}{\hbar^2}\text{Tr}_{\text{n}}\{(\mathcal{L}_{\text{zero}} + \mathcal{L}_{\text{int}})\,\text{e}^{-i\mathcal{L}\tau/\hbar}\,\mathcal{L}_{\text{zero}}\,\hat{\rho}_{\text{n}}(0)\}\end{aligned}$$

Since $\mathcal{F}_1(\tau)$ and $\mathcal{G}_{\text{zero}}(\tau)$ are only used as projection-free inputs in the Condon case, we can assume that $\mathcal{L}_{\text{int}}$ is a purely electronic superoperator, so that

https://doi.org/10.1021/acs.jpcb.1c05719
J. Phys. Chem. B 2021, 125, 9834−9852

Table 2. Bare, Static, and Dynamic Forms of the Projection-Free Inputs[a]

	bare form	static form	dynamic form
$\mathcal{K}_1(\tau)$	eq 25	$i\frac{\mathrm{d}}{\mathrm{d}\tau}\mathcal{K}_3(\tau) - \frac{1}{\hbar}\mathcal{L}_S\mathcal{K}_3(\tau)$	$\frac{\mathrm{d}}{\mathrm{d}\tau}\Phi(\tau) + \frac{i}{\hbar}\Phi(\tau)\mathcal{L}_S$
$\mathcal{K}_3(\tau)$	eq 28	eq 28	$i\dot{\mathcal{U}}_{SB}(\tau) - \frac{1}{\hbar}\mathcal{U}_{SB}(\tau)\mathcal{L}_S$
$\dot{\Phi}(\tau)$	eq 31	$i\frac{\mathrm{d}}{\mathrm{d}\tau}\mathcal{K}_3(\tau) + \frac{i}{\hbar}\dot{\mathcal{U}}_{SB}(\tau)\mathcal{L}_S - \frac{1}{\hbar^2}\mathcal{L}_S\mathcal{U}_{SB}(\tau)\mathcal{L}_S - \frac{1}{\hbar}\mathcal{L}_S\mathcal{K}_3(\tau)$	$\frac{\mathrm{d}}{\mathrm{d}\tau}\Phi(\tau)$
$\Phi(\tau)$	eq 30	$-\dot{\mathcal{U}}_{SB}(\tau) - \frac{i}{\hbar}\mathcal{L}_S\mathcal{U}_{SB}(\tau)$	eq 30
$\dot{\mathcal{F}}(\tau)$	eq 36	$\frac{\mathrm{d}}{\mathrm{d}\tau}\mathcal{G}(\tau)$	$\frac{\mathrm{d}}{\mathrm{d}\tau}\mathcal{F}(\tau)$
$\mathcal{F}(\tau)$	eq 35	$i\dot{\mathcal{U}}_M(\tau)$	eq 35
$\mathcal{F}_1(\tau)$	eq 41	$i\frac{\mathrm{d}}{\mathrm{d}\tau}\mathcal{G}_{zero}(\tau) - \frac{1}{\hbar}\mathcal{L}_{int}\mathcal{G}_{zero}(\tau)$	$i\frac{\mathrm{d}}{\mathrm{d}\tau}\mathcal{F}_2(\tau) - \frac{1}{\hbar}\mathcal{F}_2(\tau)\mathcal{L}_{int}$
$\mathcal{F}_2(\tau)$	eq 42	$i\dot{\mathcal{U}}_M(\tau) - \frac{1}{\hbar}\mathcal{L}_{int}\mathcal{U}_M(\tau)$	eq 42
$\mathcal{G}(\tau)$	eq 37	eq 37	$i\dot{\mathcal{U}}_M(\tau)$
$\mathcal{G}_{zero}(\tau)$	eq 43	eq 43	$i\dot{\mathcal{U}}_M(\tau) - \frac{1}{\hbar}\mathcal{U}_M(\tau)\mathcal{L}_{int}$

[a]This table contains the bare, static, and dynamic forms of the projection-free inputs. All of the bare forms have already been given in section 2.4, so this column only has references to the equations, while the static and dynamic columns give the explicit equation of that form, unless it is equivalent to the bare form, in which case it will also reference the equation number. In this table, numerical derivatives of projection-free inputs are indicated with $\mathrm{d}/\mathrm{d}\tau$, to differentiate from projection-free inputs that have an overdot in their symbol, that is, $\dot{\mathcal{F}}(\tau)$ and $\dot{\Phi}(\tau)$. However, the numerical first derivative of the time propagation superoperators $\mathcal{U}_{SB}(\tau)$ and $\mathcal{U}_M(\tau)$ are denoted with a single overdot for compactness. The derivations of the static and dynamic forms are given in the Supporting Information.

$$i\frac{\mathrm{d}}{\mathrm{d}\tau}\mathcal{G}_{zero}(\tau) = \underbrace{\frac{1}{\hbar^2}\mathrm{Tr}_n\{\mathcal{L}_{zero}\, e^{-i\mathcal{L}\tau/\hbar}\,\mathcal{L}_{zero}\,\hat{\rho}_n(0)\}}_{\mathcal{F}_1(\tau)} + \underbrace{\frac{1}{\hbar^2}\mathcal{L}_{int}\,\mathrm{Tr}_n\{e^{-i\mathcal{L}\tau/\hbar}\,\mathcal{L}_{zero}\,\hat{\rho}_n(0)\}}_{1/\hbar\mathcal{L}_{int}\mathcal{G}_{zero}(\tau)}$$

$\mathcal{F}_1(\tau)$ can therefore be given in terms of $\mathcal{G}_{zero}(\tau)$ and its time derivative:

$$\mathcal{F}_1^{static}(\tau) = i\frac{\mathrm{d}}{\mathrm{d}\tau}\mathcal{G}_{zero}(\tau) - \frac{1}{\hbar}\mathcal{L}_{int}\mathcal{G}_{zero}(\tau) \tag{51}$$

Equation 51 corresponds to the *static* form of $\mathcal{F}_1(\tau)$. This is because it casts $\mathcal{F}_1(\tau)$ in terms of $\mathcal{G}_{zero}(\tau)$, whose matrix elements correspond to CFs where the nuclear operators are all static:

$$\mathcal{G}_{zero,abcd}(\tau) = \frac{1}{\hbar}\mathrm{Tr}\{[\hat{H}_c\,\hat{\rho}_n(0) - \hat{\rho}_n(0)\hat{H}_d]\, e^{i\hat{H}\tau/\hbar}|b\rangle\langle a|\, e^{-i\hat{H}\tau/\hbar}\} \tag{52}$$

To obtain the *dynamic* form of $\mathcal{F}_1(\tau)$, we start out by considering the time derivative of $i\mathcal{F}_2(\tau)$ [see eq 42], which, following a procedure similar to that used to derive the static form, yields the following alternative form of $\mathcal{F}_1(\tau)$ in terms of $\mathcal{F}_2(\tau)$ and its time derivative:

$$\mathcal{F}_1^{dynamic}(\tau) = i\frac{\mathrm{d}}{\mathrm{d}\tau}\mathcal{F}_2(\tau) - \frac{1}{\hbar}\mathcal{F}_2(\tau)\mathcal{L}_{int} \tag{53}$$

Equation 53 corresponds to the *dynamic* form of $\mathcal{F}_1(\tau)$. This is because it casts $\mathcal{F}_1(\tau)$ in terms of $\mathcal{F}_2(\tau)$, whose matrix elements correspond to CFs where the nuclear operators [except for $\hat{\rho}_n(0)$] are all dynamic:

$$\mathcal{F}_{2,abcd}(\tau) = \frac{1}{\hbar}\mathrm{Tr}\{\hat{\rho}_n(0)|c\rangle\langle d|\, e^{i\hat{H}\tau/\hbar}\,[\hat{H}_a - \hat{H}_b]|a\rangle\langle b|\, e^{-i\hat{H}\tau/\hbar}\} \tag{54}$$

It should be noted that the bare, static, and dynamic forms of $\mathcal{F}_1(\tau)$ are completely interchangeable when $\mathcal{F}_1(\tau)$ is calculated via a quantum-mechanically exact method. However, the different forms can and often do differ in accuracy when calculated via approximate methods.

The bare, static, and dynamic forms of all of the projection-free inputs needed for the ten approaches under consideration in this article are summarized in Table 2. The derivations of the static and dynamic forms of the projection-free inputs are given in the Supporting Information.

Montoya-Castillo and Reichman also introduced a fourth form of the projection-free inputs in ref 33, the *propagator* form, which involves casting them in terms of the time propagation superoperator for the reduced electronic density matrix [$\mathcal{U}_{SB}(\tau) = \mathrm{Tr}_B\{e^{-i\mathcal{L}\tau/\hbar}\,\hat{\rho}_B^{eq}\}$ for the system-bath GQME and $\mathcal{U}_M(\tau) = \mathrm{Tr}_n\{e^{-i\mathcal{L}\tau/\hbar}\,\hat{\rho}_n(0)\}$ for the modified GQME] and its time derivatives. However, as was shown by Kelly et al. in ref 35, using this propagator form within the SB-PF2 approach gives back the same dynamics as the direct application of the input method used to obtain the projection-free inputs. In other words, restricting the use of the approximate method to calculating the memory kernel is

https://doi.org/10.1021/acs.jpcb.1c05719
J. Phys. Chem. B 2021, 125, 9834−9852

not expected to improve its accuracy in comparison to the direct use of the approximate method when projection-free inputs in the propagator form are used. This conclusion turns out to be true for all ten approaches under consideration in this article. Below, we demonstrate that this is the case for the M-PF-NC approach. Proofs for the other approaches are provided in the Supporting Information. In light of the fact that using the propagator form is expected to give back the same results as direct use of the approximate input method would, we refrain from reporting results for the propagator forms of the projection-free inputs for the ten approaches under consideration.

In the remainder of this section, we will show that using the propagator form within the M-PF-NC approach gives back the same dynamics as the direct application of the input method used to obtain the projection-free inputs. We start out by noting that the projection-free inputs for the M-PF-NC approach are given by $\mathcal{F}(\tau)$ and $\dot{\mathcal{F}}(\tau)$, whose bare forms are given by eqs 35 and 36, respectively. The propagator forms of $\mathcal{F}(\tau)$ and $\dot{\mathcal{F}}(\tau)$ are easily obtained by noting that $\mathcal{F}(\tau) = i\dot{\mathcal{U}}_{\mathrm{M}}(\tau) \equiv \mathcal{F}^{\mathrm{prop}}(\tau)$ and $\dot{\mathcal{F}}(\tau) = i\ddot{\mathcal{U}}_{\mathrm{M}}(\tau) \equiv \dot{\mathcal{F}}^{\mathrm{prop}}(\tau)$. Here, $\mathcal{F}^{\mathrm{prop}}(\tau)$ and $\dot{\mathcal{F}}^{\mathrm{prop}}(\tau)$ correspond to the propagator forms of $\mathcal{F}(\tau)$ and $\dot{\mathcal{F}}(\tau)$ where those projection-free inputs are given in terms of the first and second time derivatives of $\mathcal{U}_{\mathrm{M}}(\tau)$.

Next, we prove that when using the projection-free inputs in the propagator form, $\mathcal{F}^{\mathrm{prop}}(\tau)$ and $\dot{\mathcal{F}}^{\mathrm{prop}}(\tau)$, to calculate the memory kernel within the M-PF-NC approach, the dynamics generated by the modified GQME coincides with that generated by a direct application of the input method used for calculating the projection-free inputs. Proving this equivalence is facilitated by working in the energy domain, with the transformation from the time domain to the energy domain given by the Fourier-Laplace transform (FLT):

$$f(E) = \int_0^\infty \mathrm{e}^{-iEt/\hbar} f(t)\, \mathrm{d}t \tag{55}$$

It should also be noted that the FLT of the nth derivative of $f(t)$, $\frac{\mathrm{d}^n}{\mathrm{d}t^n} f(t) = f^{(n)}(t)$, is given by

$$\int_0^\infty \mathrm{e}^{-iEt/\hbar} f^{(n)}(t)\, \mathrm{d}t = \left(\frac{iE}{\hbar}\right)^n f(E) - \sum_{k=1}^{n} \left(\frac{iE}{\hbar}\right)^{n-k} f^{(k-1)}(t=0) \tag{56}$$

and that the FLT of a convolution is given by

$$\int_0^\infty \mathrm{e}^{-iEt/\hbar} \int_0^t f_1(t-\tau) f_2(\tau)\, \mathrm{d}\tau\, \mathrm{d}t = f_1(E) f_2(E) \tag{57}$$

Using eqs 55 and 56, we can find the FLT of $\mathcal{F}^{\mathrm{prop}}(\tau)$ and $\dot{\mathcal{F}}^{\mathrm{prop}}(\tau)$:

$$\mathcal{F}^{\mathrm{prop}}(E) = -\frac{E}{\hbar}\mathcal{U}_{\mathrm{M}}(E) - i \tag{58}$$

$$\dot{\mathcal{F}}^{\mathrm{prop}}(E) = -\frac{iE^2}{\hbar^2}\mathcal{U}_{\mathrm{M}}(E) + \frac{E}{\hbar} - \frac{1}{\hbar}\langle\mathcal{L}\rangle_{\mathrm{n}}^0 \tag{59}$$

where we have used the fact that $\mathcal{U}_{\mathrm{M}}(t=0)$ and $\dot{\mathcal{U}}_{\mathrm{M}}(t=0)$ are given by

$$\mathcal{U}_{\mathrm{M}}(t=0) = \mathrm{Tr}_{\mathrm{n}}\{\hat{\rho}_{\mathrm{n}}(0)\} = 1$$

$$\dot{\mathcal{U}}_{\mathrm{M}}(t=0) = -\frac{i}{\hbar}\,\mathrm{Tr}_{\mathrm{n}}\{\mathcal{L}\hat{\rho}_{\mathrm{n}}(0)\} = -\frac{i}{\hbar}\langle\mathcal{L}\rangle_{\mathrm{n}}^0$$

In the next step, we transform the Volterra equation for the memory kernel within the M-PF-NC approach, eq 46, to the energy domain:

$$\mathcal{K}^{\mathrm{M}}(E) = i\dot{\mathcal{F}}(E) - \frac{1}{\hbar}\mathcal{F}(E)\langle\mathcal{L}\rangle_{\mathrm{n}}^0 + i\mathcal{F}(E)\mathcal{K}^{\mathrm{M}}(E) \tag{60}$$

It should be noted that we used the FLT of a convolution, eq 57, in order to obtain eq 60. Rearranging eq 60, we obtain the following expression for the memory kernel in the energy domain:

$$\mathcal{K}^{\mathrm{M}}(E) = [1 - i\mathcal{F}(E)]^{-1}\left[i\dot{\mathcal{F}}(E) - \frac{1}{\hbar}\mathcal{F}(E)\langle\mathcal{L}\rangle_{\mathrm{n}}^0\right] \tag{61}$$

Plugging eqs 58 and 59 into eq 61 and simplifying, it can then be shown that

$$\mathcal{K}^{\mathrm{M,prop}}(E) = \mathcal{U}_{\mathrm{M}}{}^{-1}(E) - \Omega_{\mathrm{M}}(E) \tag{62}$$

where $\Omega_{\mathrm{M}}(E) = \frac{i}{\hbar}E + \frac{i}{\hbar}\langle\mathcal{L}\rangle_{\mathrm{n}}^0$.

Finally, transforming the modified GQME, eq 12, to the energy domain [with the help of eqs 56 and 57], we obtain

$$\frac{iE}{\hbar}\hat{\sigma}(E) - \hat{\sigma}(t=0) = -\frac{i}{\hbar}\langle\mathcal{L}\rangle_n^0\hat{\sigma}(E) - \mathcal{K}^{\mathrm{M}}(E)\hat{\sigma}(E) \tag{63}$$

Rearranging eq 63, we obtain the following expression for $\hat{\sigma}$(E)

$$\hat{\sigma}(E) = [\Omega_{\mathrm{M}}(E) + \mathcal{K}^{\mathrm{M}}(E)]^{-1}\hat{\sigma}(t=0) \tag{64}$$

Substituting $\mathcal{K}^{\mathrm{M}}(E)$ from eq 62 into eq 64 leads to the following result:

$$\hat{\sigma}^{\mathrm{prop}}(E) = [\Omega_{\mathrm{M}}(E) + \mathcal{U}_{\mathrm{M}}{}^{-1}(E) - \Omega_{\mathrm{M}}(E)]^{-1}\hat{\sigma}(t=0) = \mathcal{U}_{\mathrm{M}}(E)\hat{\sigma}(t=0) \tag{65}$$

which implies that the results obtained from the GQME will be identical to the result obtained from the direct application of the approximate method via $\mathcal{U}_{\mathrm{M}}(t)$.

3. RESULTS

In section 2.4, we introduced ten different approaches to calculating the memory kernel and in section 2.5, we outlined three forms of the projection-free inputs (bare, static, and dynamic), giving a total of 30 different pathways for calculating the memory kernel of the GQME. In this section, we compare the accuracy and numerical stability of these 30 pathways in the case of the spin-boson benchmark model and with a mapping Hamiltonian LSC approach called LSCI as the input method. We also note that LSCI has been previously referred to as the Poisson-bracket mapping equation (PBME).[43] The reader is referred ref 39 for a detailed discussion of calculating projection-free inputs via LSCI.

The spin-boson Hamiltonian is put in the form of eq 1 with $\hat{H}_j$ and $\hat{V}_{jk} \rightarrow V_{jk}$ given by

https://doi.org/10.1021/acs.jpcb.1c05719
J. Phys. Chem. B 2021, 125, 9834−9852

$$\hat{H}_1 \equiv \hat{H}_D = \epsilon + \sum_{k=1}^{N_n} \frac{\hat{P}_k^2}{2} + \frac{1}{2}\omega_k^2 \hat{R}_k^2 - c_k \hat{R}_k$$

$$\hat{H}_2 \equiv \hat{H}_A = -\epsilon + \sum_{k=1}^{N_n} \frac{\hat{P}_k^2}{2} + \frac{1}{2}\omega_k^2 \hat{R}_k^2 + c_k \hat{R}_k$$

$$V_{12} \equiv V_{DA} = V_{21} \equiv V_{AD} = \Gamma \tag{66}$$

Here, the two electronic states are designated as donor and acceptor ($|D\rangle$ and $|A\rangle$, respectively), 2ϵ is the shift in equilibrium energy between the donor (D) and acceptor (A) states, and Γ is a positive constant describing the electronic coupling between the donor and acceptor states. Since Γ is a constant, this system satisfies the Condon approximation so we can test both the non-Condon and Condon variations of the modified GQME.

For the system-bath form of the spin-boson Hamiltonian given in eq 5, we use the following commonly used definitions of the system, bath, and system−bath coupling terms:

$$\hat{H}_S = \epsilon[|D\rangle\langle D| - |A\rangle\langle A|] + \Gamma[|D\rangle\langle A| + |A\rangle\langle D|]$$

$$\hat{H}_B = \frac{1}{2}[\hat{H}_D + \hat{H}_A] = \sum_{k=1}^{N_n} \frac{\hat{P}_k^2}{2} + \frac{1}{2}\omega_k^2 \hat{R}_k^2$$

$$\hat{H}_{BS} = -\sum_{k=1}^{N_n} c_k R_k[|D\rangle\langle D| - |A\rangle\langle A|] \tag{67}$$

Following refs 38 and 39, the spectral density is assumed to be Ohmic with exponential cutoff:

$$J(\omega) = \frac{\pi}{2}\sum_{k=1}^{N_n} \frac{c_k^2}{\omega_k}\delta(\omega - \omega_k) \xrightarrow{N_n \to \infty} \frac{\pi\hbar}{2}\xi\omega\, e^{-\omega/\omega_c} \tag{68}$$

where ξ is the Kondo parameter and ω_c is the cutoff frequency. The discretization procedure to obtain the N_n nuclear mode frequencies, $\{\omega_k\}$, and coupling coefficients, $\{c_k\}$, is given in Appendix C of ref 38. The initial state of the nuclear DOF was chosen as

$$\hat{\rho}_n(0) = \frac{e^{-\beta\hat{H}_B}}{\mathrm{Tr}_B\{e^{-\beta\hat{H}_B}\}} = \frac{e^{-\beta(\hat{H}_D+\hat{H}_A)/2}}{\mathrm{Tr}_n\{e^{-\beta(\hat{H}_D+\hat{H}_A)/2}\}} \tag{69}$$

It should be noted that this particular choice is dictated by our desire to compare the modified approaches to the system-bath approaches, which require that the initial nuclear state corresponds to thermal equilibrium with respect to the bath Hamiltonian, by definition. At the same time, it is also important to emphasize that the modified approaches are designed to accommodate arbitrary initial nuclear states of one's choice.

Calculations were carried out for three different sets of parameter values adopted from refs 38 and 39 (see Table 3). Models 1 and 2 differ only in the value of the cutoff frequency, and model 3 corresponds to an unbiased, weakly coupled system at a higher temperature. The numerical integration scheme was adopted from ref 39. The results reported in this article were obtained with a time step of Δt = 0.001 Γ^{-1} and by averaging over 10^6 trajectories for each pathway and model. Quantum-mechanically exact results were adopted from ref 34 for models 1 and 2 and from ref 44 for model 3. Numerical derivatives were calculated with the fourth-order central finite difference method.

Table 3. Spin-Boson Model and Simulation Parameters

	model parameters					numerical parameters		
model no.	ϵ	Γ	β	ξ	ω_c	ω_{max}	N_n	Δt
1	1.0	1.0	5.0	0.1	1.0	5	400	0.001
2	1.0	1.0	5.0	0.1	2.0	10	400	0.001
3	0.0	$0.\overline{333}$	3.0	0.1	1.0	5	400	0.001

The following paragraphs describe the behavior of each pathway for the three models from Table 3, as seen in their corresponding figures. A summary of the results is given in Table 4. Section 4 will discuss the possible causes for the differing behavior of the pathways described in this section.

Shown in Figure 3 are the electronic population difference results, $\sigma_z(t) = \sigma_{DD}(t) - \sigma_{AA}(t)$, for each approach with the bare, static, and dynamic forms for model 1 in Table 3 with a memory time of 20 Γ^{-1}. For better visibility, the results are divided between the system-bath approaches (left panels) and the modified approaches (right panels) and between the bare (top panels), static (middle panels), and dynamic (bottom panels) forms for a total of six graphs. The results in Figure 3 show that for model 1 there is no difference between the bare and static forms within each approach, while the dynamic form gives back the same results as the direct application of LSCI for all approaches. For the bare and static forms, all the projection-first approaches (i.e., SB-PF1, SB-PF2, M-PF-NC, and M-PF-C) yield accurate results for model 1. SB-TE and SB-PS yield the same slightly larger amplitudes than the exact results, while M-TE-NC and M-PS-NC give the same damped results compared to the exact results. The M-PS-C approach also gives damped oscillations compared to the exact results, though they are slightly less damped than the M-TE-NC and M-PS-NC approaches. The M-TE-C gives results that trend below the exact results.

Shown in Figure 4 are the electronic population difference results for each approach with the bare, static, and dynamic forms for model 2 in Table 3 with a memory time of 20 Γ^{-1}. Compared to model 1, model 2 has a higher ω_c, and therefore quantum nuclear effects are expected to be more pronounced. Thus, the classical treatment of the nuclear DOF within LSCI is expected to be less valid, which leads to bigger differences between the results obtained via different pathways (see Figure 4). This is consistent with previously seen results in refs 38 and 39. The results in Figure 4 show that for model 2 as well there is no difference between the bare and static forms within each approach, while the dynamic form gives the same dynamics as LSCI regardless of approach. With the bare and static forms, the most accurate approaches are the projection-first approaches (i.e., SB-PF1, SB-PF2, M-PF-NC, and M-PF-C), which are in excellent agreement with the exact results. SB-TE and SB-PS again have larger oscillations than the exact results, with a more significant difference than in model 1. The M-TE-NC and M-PS-NC approaches give damped oscillations that trend above the exact results. The M-TE-C and M-PS-C approaches give damped oscillations.

Shown in Figure 5 are the electronic population difference results for each approach with the bare, static, and dynamic forms for model 3 in Table 3 with a memory time of 20 Γ^{-1}. The results in Figure 5 show that for model 3 there is no difference between the bare and static forms within each

https://doi.org/10.1021/acs.jpcb.1c05719
J. Phys. Chem. B 2021, 125, 9834−9852

Table 4. Comparison of Results Obtained with the Bare and Static Forms[a]

Approach	Accuracy			Converged with Increasing Memory Time			Number of Equations	Static or Dynamic Nuclear Operator(s)
	Model #			Model #				
	1	2	3	1	2	3		
SB-TE	✓̸	×	✓	✓̸	×	×	Two	Both
								Static
SB-PF1	✓	✓	✓	✓	✓	✓	One	Both
								Dynamic
SB-PF2	✓	✓	✓	✓	✓	✓	One	Both
								Dynamic
SB-PS	✓̸	×	✓	✓̸	×	×	One	Both
								Static
M-TE-NC	×	×	×	✓̸	×	×	Two	Both
								Static
M-TE-C	×	✓̸	✓	×	×	✓	Two	Both
								Dynamic
								Static
M-PF-NC	✓	✓	✓	✓	✓	✓	One	Both
								Dynamic
M-PF-C	✓	✓	✓	✓	✓	✓	One	Both
								Dynamic
M-PS-NC	×	×	×	✓̸	×	×	One	Both
								Static
M-PS-C	×	✓̸	✓	×	×	✓̸	One	Both
								Static

[a]In the *accuracy* column, the accuracy of each approach is given, with check marks indicating that the approach is accurate, slashed check marks indicating slight deviations from the exact results, and × indicating significant deviations from the exact results. In the *converged with increasing memory time*column, the stability with increasing memory time is given, with check marks indicating that the approach converges with increasing memory time, slashed check marks indicating that the approach becomes slightly unstable with increasing memory time, and × indicating that the approach becomes significantly unstable with increasing memory time. The last two columns (also given in Table 1) are included to help facilitate the discussion of the results.

approach, while the dynamic forms of all approaches give the same dynamics as LSCI, consistent with models 1 and 2. Within the short time scale for which exact results are available, the bare and static forms of all the approaches except the M-TE-NC and M-PS-NC yield accurate dynamics. However, we also see differences between the approaches at longer times, with SB-TE and SB-PS having larger amplitudes than the SB-PF1 and SB-PF2. This is similar to models 1 and 2, where the SB-PF1 and SB-PF2 approaches were observed to be accurate at long times (see Figures 3 and 4). M-TE-C, M-PF-NC, and M-PF-C give similar results to SB-PF1 and SB-PF2 at long times, while M-PS-C gives larger oscillations similar to SB-TE and SB-PS.

Shown in Figures 6, 8, and 10 are the results obtained for the system-bath approaches with the bare form at memory times increasing by 2 Γ^{-1} from 6 Γ^{-1} to 20 Γ^{-1} for models 1, 2, and 3 in Table 3, respectively. The results for the static form are the same as the bare form (not shown). The SB-PF1 and SB-PF2 approaches yield converged results with increasing memory time, while SB-TE and SB-PS do not, particularly for model 2. This is consistent with previously shown results for the spin-boson model with SB-TE, SB-PF1, and M-PF-C in ref 38 and for a model of the FMO complex with SB-TE and M-PF-C in ref 40. In those references, the projection-free inputs were obtained with the Ehrenfest method rather than LSCI, and the SB-TE approach also did not give converged results with increasing memory time, while the SB-PF1 and M-PF-C results were converged.

Shown in Figures 7, 9, and 11 are the results of the modified approaches with the bare form at memory times increasing by 2 Γ^{-1} from 6 Γ^{-1} to 20 Γ^{-1} for models 1, 2, and 3 in Table 3, respectively. The results for the static form are the same as the bare form (not shown). The M-PF-NC and M-PF-C approaches are seen to converge with increasing memory time for all models. M-TE-NC and M-PS-NC do not give converged results with increasing memory time, particularly for models 2 and 3. The M-PS-C approach also does not give converged results with increasing memory time, particularly for models 1 and 2. The M-TE-C approach gives unconverged results for models 1 and 2, while it gives converged results for model 3 with increasing memory time.

The results of increasing the memory time with the dynamic form are not shown because they converged for all approaches.

In Table 4, the results of the bare and static forms from Figures 3−11 are summarized, and two columns with details about the approaches from Table 1 are included to help facilitate the discussion of the results in section 4. The dynamic form results are not included because all approaches give back the same dynamics as the input method and converge with increasing memory time.

4. DISCUSSION

Comparing and contrasting the results obtained via the different pathways for calculating the memory kernel and projection-free inputs in the previous section gives rise to

https://doi.org/10.1021/acs.jpcb.1c05719
J. Phys. Chem. B 2021, 125, 9834−9852

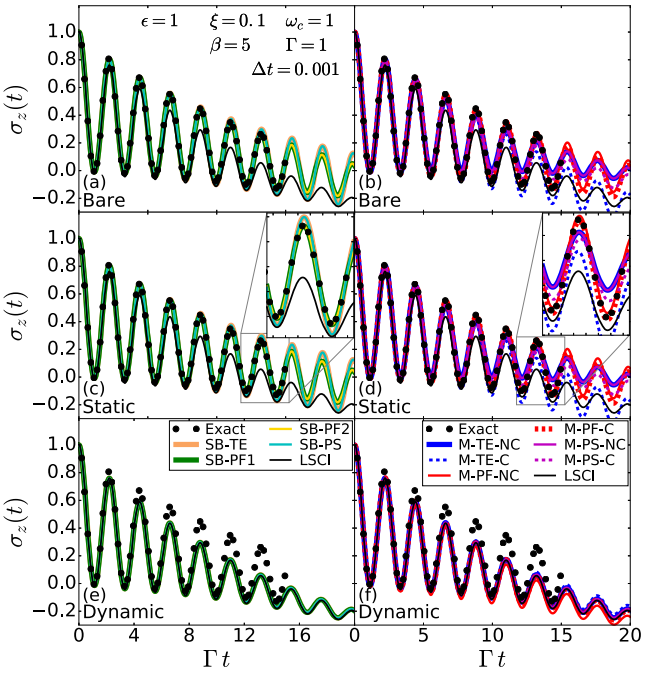

Figure 3. Electronic population difference, $\sigma_z(t) = \sigma_{DD}(t) - \sigma_{AA}(t)$, for model 1 in Table 3 with a memory time of 20 Γ^{-1}. Shown are the results of (a) bare form of system-bath approaches, (b) bare form of modified approaches, (c) static form of system-bath approaches, (d) static form of modified approaches, (e) dynamic form of system-bath approaches, and (f) dynamic form of modified approaches. On graphs c and d, a magnified inset is included to help distinguish between the approaches. There is no difference between the results of the bare and static forms and the projection-first approaches yield the most accurate results.

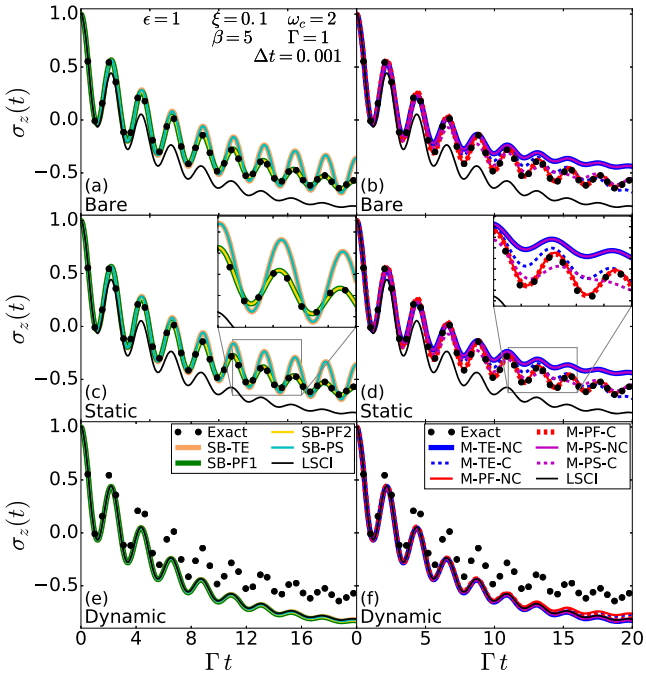

Figure 4. Electronic population difference, $\sigma_z(t) = \sigma_{DD}(t) - \sigma_{AA}(t)$, for model 2 in Table 3 with a memory time of 20 Γ^{-1}. Shown are the results of (a) bare form of system-bath approaches, (b) bare form of modified approaches, (c) static form of system-bath approaches, (d) static form of modified approaches, (e) dynamic form of system-bath approaches, and (f) dynamic form of modified approaches. On graphs c and d, a magnified inset is included to help distinguish between the approaches. There is no difference between the results of the bare and static forms and the projection-first approaches yield the most accurate results.

several valuable insights, which are summarized in the following subsections.

4.1. Pathways of Choice. While the bare and static forms of the TE and PS approaches were able to give accurate and numerically stable results for model 3, the bare and static forms of the PF approaches gave accurate and numerically stable results for all three models. Combining this with the disadvantages of the system-bath form outlined in section 2.1 seems to point to the bare and static forms of M-PF-NC and M-PF-C as the pathways of choice.

4.2. System-Bath GQME vs Modified GQME. Looking at the bare and static forms of the projection-free inputs, for the two-equation and projection-second approaches, the system-bath approaches (SB-TE and SB-PS) give rise to larger oscillations than the exact results. Among the modified approaches, the non-Condon approaches (M-TE-NC and M-PS-NC) have smaller oscillations and can be shifted from the exact results, and the Condon approaches (M-TE-C and M-PS-C) tend to outperform their system-bath and non-Condon equivalents, though they are still unable to quantitatively capture the exact results for two of the three models.

In contrast, the projection-first approaches gave rise to accurate results for both the system-bath approaches (SB-PF1 and SB-PF2) and the modified approaches (M-PF-NC and M-PF-C). Thus, the accuracy appears to be affected most strongly by whether one expresses the memory kernel in terms of an exponential operator where the projection operator precedes the Liouvillian [projection-first (PF) approaches] or the other way around [projection-second (PS) approaches], rather than by whether one uses the system-bath or modified forms of the GQME (with the projection-first approaches being significantly more accurate). However, considering the disadvantages of the system-bath form outlined in section 2.1, it can still be argued that the modified form of the GQME is preferable to the system-bath form for systems whose Hamiltonian has the form of eq 1.

4.3. Effect of Number of Equations for the Memory Kernel. The SB-TE and SB-PS approaches and the M-TE-NC and M-PS-NC approaches share the same projection-free inputs but correspond to a different number of equations needed to obtain the memory kernel (see Table 1). The TE approaches require first calculating a projection-dependent input with a Volterra equation before calculating the memory kernel with an equation of the projection-free and projection-dependent inputs. In contrast, the PS approaches have a single Volterra equation for the memory kernel. As shown in Figures 3−5, this difference in number of equations does not affect the accuracy of the results. The M-TE-C and M-PS-C approaches do give different results, but the M-TE-C approach contains a projection-free input that the M-PS-C approach does not have (see Table 1). This observation suggests that it is the projection-free inputs that effect the differences between the approaches, rather than the number of equations needed to get the memory kernel from them.

4.4. Effect of the Projection-Free Inputs and Their Forms on Accuracy and Convergence. In this section, we point out correlations between the type and form of the projection-free inputs and the accuracy and numerical

https://doi.org/10.1021/acs.jpcb.1c05719
J. Phys. Chem. B 2021, 125, 9834−9852

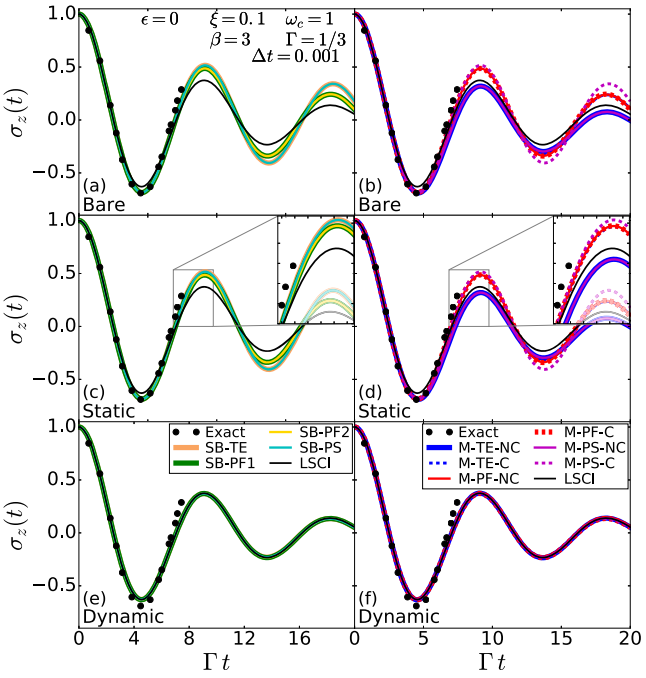

Figure 5. Electronic population difference, $\sigma_z(t) = \sigma_{DD}(t) - \sigma_{AA}(t)$, for model 3 in Table 3 with a memory time of 20 Γ^{-1}. Shown are the results of (a) bare form of system-bath approaches, (b) bare form of modified approaches, (c) static form of system-bath approaches, (d) static form of modified approaches, (e) dynamic form of system-bath approaches, and (f) dynamic form of modified approaches. On graphs c and d, a magnified inset is included to help distinguish between the approaches. There is no difference between the results of the bare and static forms and the projection-first approaches yield the most accurate results.

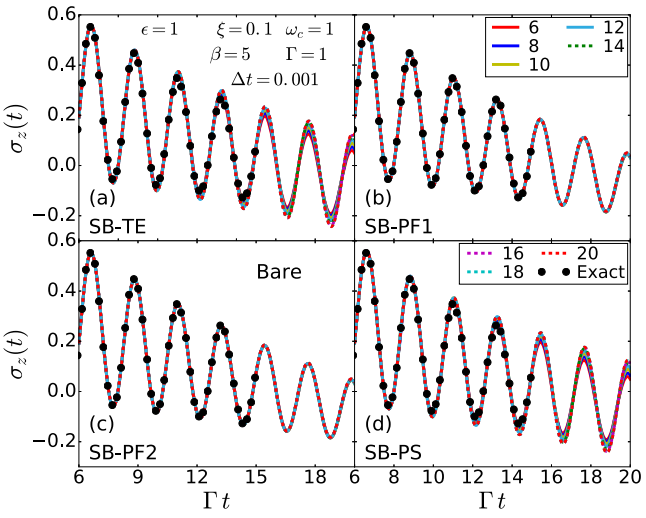

Figure 6. Electronic population difference, $\sigma_z(t) = \sigma_{DD}(t) - \sigma_{AA}(t)$, as a function of memory time for the system-bath approaches with the bare form for model 1 in Table 3: (a) SB-TE approach, (b) SB-PF1 approach, (c) SB-PF2 approach, and (d) SB-PS approach. The memory times are given in the legends in units of Γ^{-1}. SB-PF1 and SB-PF2 are seen to converge with increasing memory time, while SB-TE and SB-PS become slightly unstable with increasing memory time.

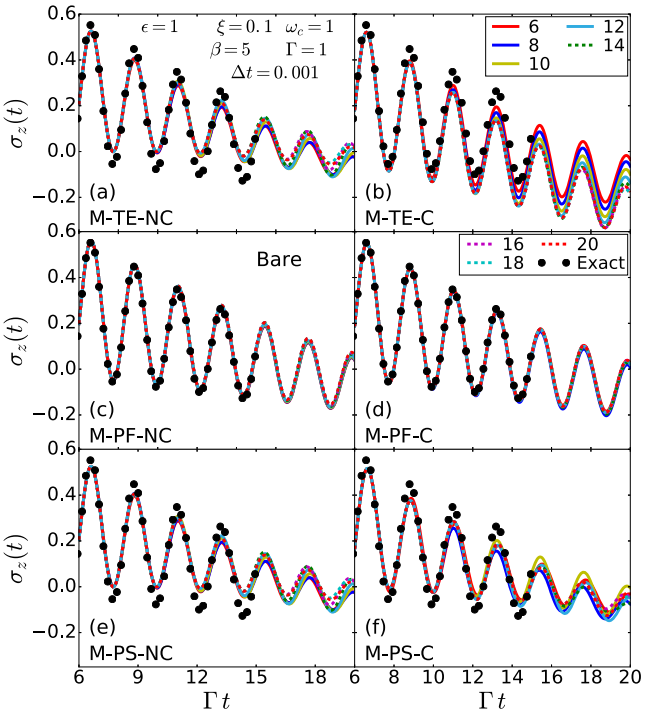

Figure 7. Electronic population difference, $\sigma_z(t) = \sigma_{DD}(t) - \sigma_{AA}(t)$, as a function of memory time for the modified approaches with the bare form for model 1 in Table 3: (a) M-TE-NC, (b) M-TE-C, (c) M-PF-NC, (d) M-PF-C, (e) M-PS-NC, and (f) M-PS-C. The memory times are given in the legends in units of Γ^{-1}. M-PF-NC and M-PF-C are seen to converge with increasing memory time, M-TE-NC and M-PS-NC are seen to be slightly unstable with increasing memory time, and M-TE-C and M-PS-C are seen to be significantly unstable with increasing memory time.

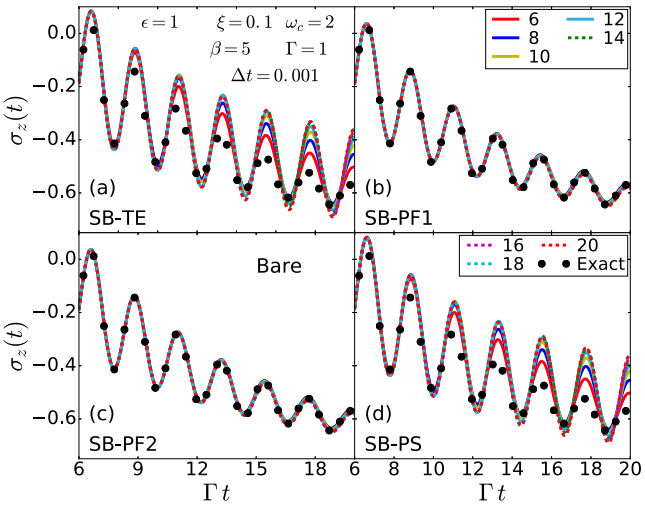

Figure 8. Electronic population difference, $\sigma_z(t) = \sigma_{DD}(t) - \sigma_{AA}(t)$, as a function of memory time for the system-bath approaches with the bare form for model 2 in Table 3: (a) SB-TE, (b) SB-PF1, (c) SB-PF2, and (d) SB-PS. The memory times are given in the legend in units of Γ^{-1}. SB-PF1 and SB-PF2 are seen to converge with increasing memory time, while SB-TE and SB-PS are seen to be significantly unstable with increasing memory time.

stability of the results. To this end, we will use Table 5, which summarizes the integral equations used to obtain the memory kernel within each pathway. The integral equations are broken down into their linear terms (LTs) and integral terms (ITs). For example, looking at the Volterra equation of the M-PF-NC approach given in eq 46, it contains two linear terms and one integral term:

https://doi.org/10.1021/acs.jpcb.1c05719
J. Phys. Chem. B 2021, 125, 9834−9852

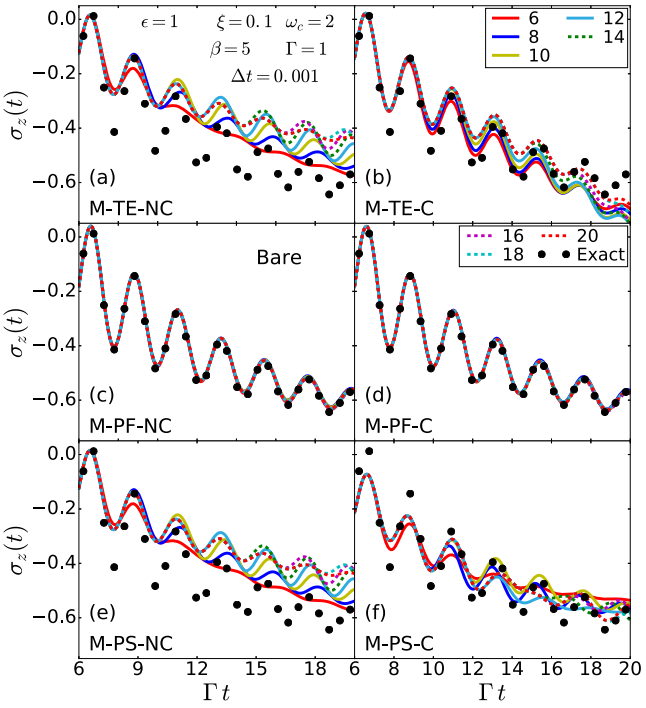

Figure 9. Electronic population difference, $\sigma_z(t) = \sigma_{DD}(t) - \sigma_{AA}(t)$, as a function of memory time for the modified approaches with the bare form for model 2 in Table 3: (a) M-TE-NC, (b) M-TE-C, (c) M-PF-NC, (d) M-PF-C, (e) M-PS-NC, and (f) M-PS-C. The memory times are given in the legend in units of Γ^{-1}. M-PF-NC and M-PF-C are seen to converge with increasing memory time; M-TE-C is seen to be slightly unstable with increasing memory time; and M-TE-NC, M-PS-NC, and M-PS-C are seen to be significantly unstable with increasing memory time.

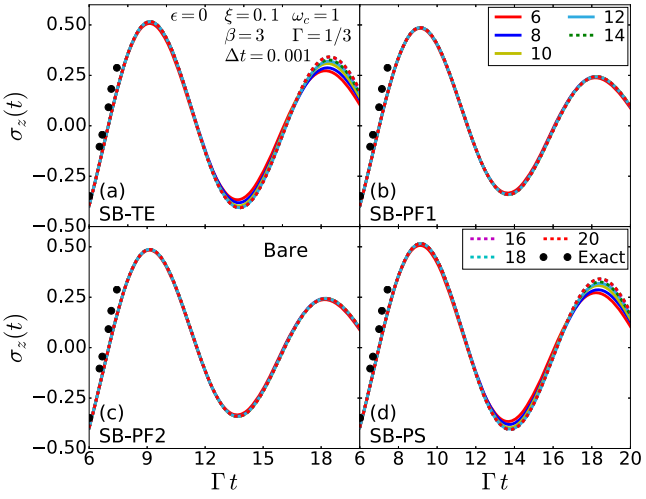

Figure 10. Electronic population difference, $\sigma_z(t) = \sigma_{DD}(t) - \sigma_{AA}(t)$, as a function of memory time for the system-bath approaches with the bare form for model 3 in Table 3: (a) SB-TE, (b) SB-PF1, (c) SB-PF2, and (d) SB-PS. The memory times are given in the legends in units of Γ^{-1}. SB-PF1 and SB-PF2 are seen to converge with increasing memory time, while SB-TE and SB-PS are slightly unstable.

$$\mathcal{K}^{M}(\tau) = \underbrace{i\dot{\mathcal{F}}(\tau)}_{LT} - \underbrace{\frac{1}{\hbar}\mathcal{F}(\tau)\langle\mathcal{L}\rangle_n^0}_{LT} + i\int_0^\tau d\tau' \underbrace{\mathcal{F}(\tau-\tau')}_{IT}\mathcal{K}^{M}(\tau')$$

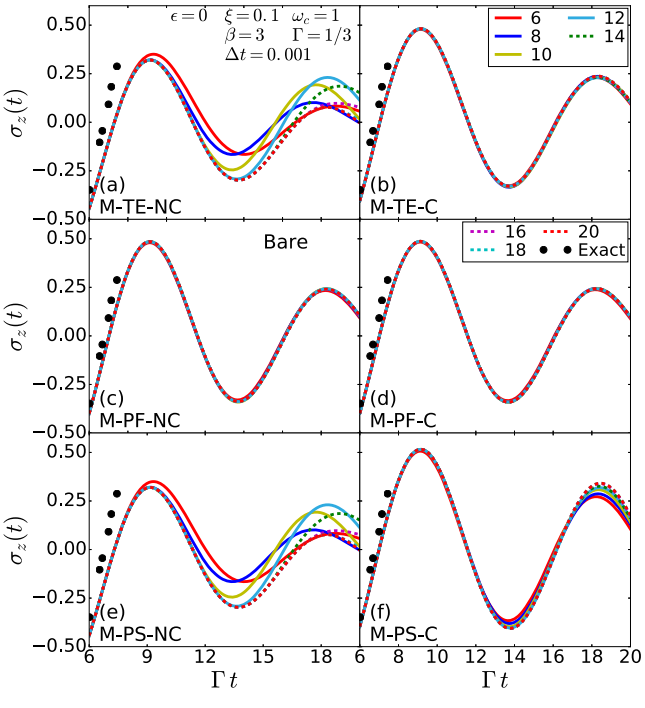

Figure 11. Electronic population difference, $\sigma_z(t) = \sigma_{DD}(t) - \sigma_{AA}(t)$, as a function of memory time for the modified approaches with the bare form for model 3 in Table 3: (a) M-TE-NC, (b) M-TE-C, (c) M-PF-NC, (d) M-PF-C, (e) M-PS-NC, and (f) M-PS-C. The memory times are given in the legends in units of Γ^{-1}. M-PF-NC, M-PF-C, and M-TE-C are seen to converge with increasing memory time; M-PS-C is seen to be slightly unstable with increasing memory time; and M-TE-NC and M-PS-NC are seen to be significantly unstable with increasing memory time.

The explicit expressions for the memory kernels of each pathway are given in the Supporting Information.

Inspection of the results in section 3 reveals two main trends:

1 The bare and static forms of the projection-free inputs result in GQME-based results that are significantly more accurate compared to direct application of LSCI, while the dynamic form gives back GQME-based results that are the same as the results obtained via direct application of LSCI.
2. While the bare and static forms of the PF approaches exhibit stable behavior with increasing memory time, the bare and static forms of the TE and PS approaches do not.

Matching these to trends in Table 5, we see that

1. For all approaches, the bare and static forms of the memory kernel Volterra equations always have at least one projection-free input with either both static and dynamic nuclear operators (purple in Table 5) or only static nuclear operators (teal in Table 5) in their LTs, while the dynamic form never has projection-free inputs with static nuclear operators in its LTs.
2. The bare and static forms of the TE and PS approaches always have at least one projection-free input with both static and dynamic nuclear operators (purple in Table 5) or only static nuclear operators (teal in Table 5) in their ITs, while the PF approaches never have projection-free inputs containing static nuclear operators in their ITs.

https://doi.org/10.1021/acs.jpcb.1c05719
J. Phys. Chem. B 2021, 125, 9834−9852

Table 5. Comparison of the Pathways' Integral Equations for the Memory Kernels[a]

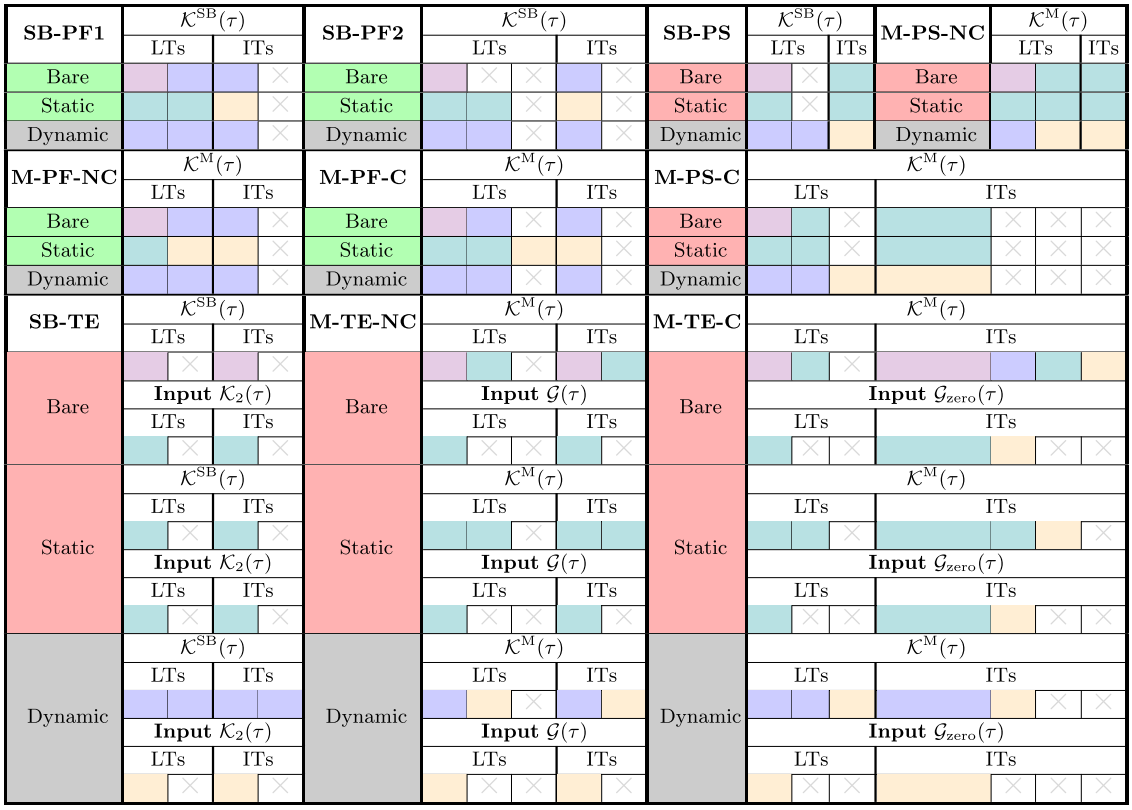

[a]In this table, we compare the integral equations used to obtain the memory kernel (and projection-dependent input, for the TE approaches) for each pathway. The Volterra equation for the memory kernel (and projection-dependent input for the TE approaches) are given in a column to the right of the title of the pathway. The Volterra equations are broken down into their linear terms (LTs) and integral terms (ITs). Terms with projection-free inputs which contain both a static and a dynamic nuclear operator [i.e., $\mathcal{K}_1(\tau)$, $\dot{\Phi}(\tau)$, $\dot{\mathcal{F}}(\tau)$, and $\mathcal{F}_1(\tau)$] are highlighted by a purple rectangle; terms with projection-free inputs that contain only a static nuclear operator [i.e., $\mathcal{K}_3(\tau)$, $\mathcal{G}(\tau)$, and $\mathcal{G}_{zero}(\tau)$] are highlighted by a teal rectangle; terms with projection-free inputs that contain only a dynamic nuclear operator [i.e., $\Phi(\tau)$, $\mathcal{F}(\tau)$, and $\mathcal{F}_2(\tau)$] are highlighted by a blue rectangle; and terms containing only the time propagation superoperator [i.e., $\mathcal{U}_{SB}(\tau)$ or $\mathcal{U}_{M}(\tau)$] or its time derivatives are highlighted by a beige rectangle. For each form, the average of the memory-time convergence for the three models are color-coded, with green representing stable results and red representing unstable results with increasing memory time, while gray represents that the form was stable but did not give any accuracy benefit over the input method. We can see that green forms always have at least one projection-free input with either both static and dynamic nuclear operators (purple) or only static nuclear operators (teal) in their LTs and no projection-free inputs with a static nuclear operator (purple or teal) in their ITs, while the red forms have at least one projection-free input with either both static and dynamic nuclear operators (purple) or only static nuclear operators (teal) in their LTs and ITs. The gray forms have no projection-free inputs with both static and dynamic nuclear operators (purple) or only static nuclear operators (teal) in their LTs or ITs.

Addressing the first trend, in ref 33, Montoya-Castillo and Reichman argued that the reason for why the bare and static forms provided improvements in accuracy for the SB-PF1 and SB-PS approaches (with Ehrenfest as input method) was that the sampling of the static nuclear operators provides additional information about the system-bath interaction that the direct application of Ehrenfest and the dynamic form do not. Our results show that this trend extends to other approaches and another input method, thereby reinforcing the importance of static nuclear operators in providing accuracy improvements. Montoya-Castillo and Reichman also argued that dynamic nuclear operators could introduce error due to their oscillatory nature. However, examining approaches in which all projection-free inputs contain dynamic nuclear operators in the bare form (i.e., SB-PF1, SB-PF2, M-PF-NC, and M-PF-C) reveals no difference between the bare and static results. It therefore appears that at least for the system under consideration here, any errors introduced by dynamic nuclear operators are negligible.

Addressing the second trend, we note that the fact that certain pathways converge with increasing memory time while others do not has been observed in our previous papers.[38,40] As stated above, within the integral equations for the memory kernel, the bare and static forms of the TE and PS approaches always have at least one projection-free input containing static nuclear operators in the integral terms, while the PF approaches never do. It should be noted that the integral term corresponds to a convolution of the memory kernel and a projection-free input quantity. Based on the appearance of long-time oscillations in the memory kernel of the bare and static forms of the TE and PF approaches (with graphs provided in the Supporting Information and this trend noted also in ref 38), a static nuclear operator projection-free input appears to overlap more with the memory kernel at long times.

While these observations are based on results obtained for the spin-boson model with LSCI as the input method, they are consistent with similar observations in the case of the

https://doi.org/10.1021/acs.jpcb.1c05719
J. Phys. Chem. B 2021, 125, 9834−9852

spin-boson model with Ehrenfest as the input method[33,38] and in the FMO complex with Ehrenfest as the input method,[40] indicating that these could be general trends. Additional study with different systems, spectral densities, and input methods would be needed to verify the generality of these trends.

5. CONCLUSIONS

The GQME provides a general framework for simulating electronic energy, charge, and coherence transfer dynamics in molecular systems. Within this framework, the effect of the nuclear DOF on the time evolution of the electronic reduced density matrix is fully captured by a memory kernel superoperator. Multiple pathways for calculating the memory kernel of the GQME from projection-free inputs have been proposed over the past two decades. These pathways differ with respect to the actual memory kernel, which depends on the choice of projection operator, the way in which the memory kernel is calculated, and the form of the projection-free inputs used for calculating it. Regardless of these differences, all of those pathways are expected to generate the same electronic energy, charge, and coherence transfer dynamics *when the projection-free inputs are calculated in a quantum-mechanically exact manner*. However, such a quantum-mechanically exact approach is not feasible for many systems of practical interest. As a result, approximate semiclassical and mixed quantum-classical methods are used instead for calculating the projection-free inputs, which leads to a situation where different pathways for calculating the memory kernel can and often do give rise to results that differ in accuracy as well as numerical stability.

In this article, we mapped out 30 different pathways to calculating the memory kernel of the GQME. Those 30 pathways are based on combining ten different approaches to calculating the memory kernel with three different forms (bare, static, and dynamic) of the projection-free inputs. To the best of our knowledge, while some of those pathways have been previously proposed and applied (the bare forms of SB-TE, SB-PF1, M-PF-NC, and M-PF-C and all forms of SB-PF2 and SB-PS), others are introduced here for the first time (the static and dynamic forms of SB-TE, SB-PF1, M-PF-NC, and M-PF-C and all forms of M-TE-NC, M-TE-C, M-PS-NC, and M-PS-C). We have also compared and contrasted results obtained via those 30 different pathways for a benchmark spin-boson model with three sets of parameters and the approximate LSCI as the input method. The results clearly show notable differences in accuracy and numerical stability between the pathways, thereby demonstrating that the choice of pathway can be critical for the success of a GQME-based approach.

Analysis of the results obtained for the spin-boson model with LSCI as the input method suggests that there are two choices that make the most difference when it comes to the accuracy and numerical stability of the GQME-based approach. One important choice is the form of the projection-free inputs, with pathways based on the bare and static forms outperforming pathways based on the dynamic form. This is likely due to additional information about the system-bath interaction that static nuclear operators provide. Another important choice is the order in which the projection operator and Liouvillian appear in the exponential operator within the memory kernel. More specifically, projection-first (PF) pathways, where the projection operator precedes the Liouvillian, seem to yield the most accurate as well as the most numerically stable results, while projection-second (PS) pathways, where the Liouvillian precedes the projection operator, tend to be either inaccurate or numerically unstable or both.

We view the results of the comprehensive analysis presented in this article as encouraging, since certain pathways clearly demonstrate the gains in accuracy and computational cost that can be achieved by restricting the use of approximate methods to calculating the memory kernel, over their direct application for simulating the dynamics of the overall system. At the same time, it is also clear that not all pathways were created equal and that some may offer no advantage over direct application or give rise to numerical instabilities.

The results and analysis presented in this article, as well as related observations made in refs 38−40 seem to point to the modified projection-first non-Condon (M-PF-NC) and Condon (M-PF-C) as the pathways of choice. Additional theoretical analysis as well as applications to other systems and spectral densities with a wider variety of approximate input methods would be necessary in order to establish the generality of those observations or lack thereof. Work on such extensions is currently underway in our group and will be reported in future publications.

■ ASSOCIATED CONTENT

Supporting Information

The Supporting Information is available free of charge at https://pubs.acs.org/doi/10.1021/acs.jpcb.1c05719.

> Additional technical details, including the derivations of the memory kernel and intermediate Volterra equation of the M-TE-C approach, the derivations of the static and dynamic forms of the projection-free inputs for each of the approaches along with descriptions and derivations of the propagator form from ref 30, the integral equations for the memory kernel and projection-dependent inputs for the bare, static, and dynamic forms of each approach, graphs of selected memory kernel elements for each model, and the FLTs of the projection-free inputs and the derivation of the FLTs of the memory kernels and GQMEs of each of the approaches and forms (PDF)

■ AUTHOR INFORMATION

Corresponding Author

Eitan Geva − *Department of Chemistry, University of Michigan, Ann Arbor, Michigan 48109, United States;* orcid.org/0000-0002-7935-4586; Email: eitan@umich.edu

Author

Ellen Mulvihill − *Department of Chemistry, University of Michigan, Ann Arbor, Michigan 48109, United States*

Complete contact information is available at: https://pubs.acs.org/10.1021/acs.jpcb.1c05719

Notes

The authors declare no competing financial interest.

■ ACKNOWLEDGMENTS

E.G. acknowledges support from the NSF via Grant No. CHE-1800325 and computational resources and services provided by the Advanced Research Computing at the University of Michigan, Ann Arbor.

■ REFERENCES

(1) Xu, D.; Schulten, K. Coupling of protein motion to electron transfer in a photosynthetic reaction center: investigating the low temperature behavior in the framework of the spin−boson model. *Chem. Phys.* **1994**, *182*, 91−117.
(2) Ishizaki, A.; Fleming, G. R. Quantum Coherence in Photosynthetic Light Harvesting. *Annu. Rev. Condens. Matter Phys.* **2012**, *3*, 333−361.
(3) Liddell, P. A.; Kuciauskas, D.; Sumida, J. P.; Nash, B.; Nguyen, D.; Moore, A. L.; Moore, T. A.; Gust, D. Photoinduced charge separation and charge recombination to a triplet state in a carotene-porphyrin-fullerene triad. *J. Am. Chem. Soc.* **1997**, *119*, 1400−1405.
(4) Liddell, P. A.; Kodis, G.; Moore, A. L.; Moore, T. A.; Gust, D. Photo switching of photoinduced electron transfer in a dithienylethene-porphyrin-fullerene triad molecule. *J. Am. Chem. Soc.* **2002**, *124*, 7668−7669.
(5) Brédas, J.-L.; Beljonne, D.; Coropceanu, V.; Cornil, J. Charge-Transfer and Energy-Transfer Processes in π-Conjugated Oligomers and Polymers: A Molecular Picture. *Chem. Rev.* **2004**, *104*, 4971−5004.
(6) Rizzi, A. C.; van Gastel, M.; Liddell, P. A.; Palacios, R. E.; Moore, G. F.; Kodis, G.; Moore, A. L.; Moore, T. A.; Gust, D.; Braslavsky, S. E. Entropic changes control the charge separation process in triads mimicking photosynthetic charge separation. *J. Phys. Chem. A* **2008**, *112*, 4215−4223.
(7) Tian, H.; Yu, Z.; Hagfeldt, A.; Kloo, L.; Sun, L. Organic Redox Couples and Organic Counter Electrode for Efficient Organic Dye-Sensitized Solar Cells. *J. Am. Chem. Soc.* **2011**, *133*, 9413−9422.
(8) Mishra, A.; Fischer, M. K. R.; Bäuerle, P. Metal-Free Organic Dyes for Dye-Sensitized Solar Cells: From Structure: Property Relationships to Design Rules. *Angew. Chem., Int. Ed.* **2009**, *48*, 2474−2499.
(9) Feldt, S. M.; Gibson, E. A.; Gabrielsson, E.; Sun, L.; Boschloo, G.; Hagfeldt, A. Design of Organic Dyes and Cobalt Polypyridine Redox Mediators for High-Efficiency Dye-Sensitized Solar Cells. *J. Am. Chem. Soc.* **2010**, *132*, 16714−16724.
(10) Zhao, Y.; Liang, W. Charge transfer in organic molecules for solar cells: Theoretical perspective. *Chem. Soc. Rev.* **2012**, *41*, 1075−1087.
(11) Lee, M. H.; Dunietz, B. D.; Geva, E. Calculation From First Principles of Intramolecular Golden-Rule Rate Constants for Photo-Induced Electron Transfer in Molecular Donor-Acceptor Systems. *J. Phys. Chem. C* **2013**, *117*, 23391−23401.
(12) Lee, M. H.; Dunietz, B. D.; Geva, E. Donor-to-Donor vs. Donor-to-Acceptor Interfacial Charge Transfer States in the Phthalocyanine-Fullerene Organic Photovoltaic System. *J. Phys. Chem. Lett.* **2014**, *5*, 3810−3816.
(13) Meyer, H.-D.; Gatti, F.; Worth, G. A.*Multidimensional Quantum Dynamics: MCTDH Theory and Applications*; John Wiley & Sons, 2009.
(14) Makri, N. Time-dependent quantum methods for large systems. *Annu. Rev. Phys. Chem.* **1999**, *50*, 167.
(15) Jin, J.; Zheng, X.; Yan, Y. Exact dynamics of dissipative electronic systems and quantum transport: Hierarchical equations of motion approach. *J. Chem. Phys.* **2008**, *128*, 234703−16.
(16) Tanimura, Y.; Kubo, R. Time evolution of a quantum system in contact with a nearly Gaussian-Markoffian noise bath. *J. Phys. Soc. Jpn.* **1989**, *58*, 101.
(17) Tanimura, Y. Nonperturbative expansion method for a quantum system coupled to a harmonic-oscillator bath. *Phys. Rev. A: At., Mol., Opt. Phys.* **1990**, *41*, 6676−6687.
(18) Tanimura, Y. Stochastic Liouville, Langevin, Fokker−Planck, and Master Equation Approaches to Quantum Dissipative Systems. *J. Phys. Soc. Jpn.* **2006**, *75*, 082001−39.
(19) Greene, S. M.; Batista, V. S. Tensor-Train Split-Operator Fourier Transform (TT-SOFT) Method: Multidimensional Nonadiabatic Quantum Dynamics. *J. Chem. Theory Comput.* **2017**, *13*, 4034−4042.
(20) Nakajima, S. On the quantum theory of transport phenomena. *Prog. Theor. Phys.* **1958**, *20*, 948−959.
(21) Zwanzig, R. Ensemble method in the theory of irreversibility. *J. Chem. Phys.* **1960**, *33*, 1338−1341.
(22) Shi, Q.; Geva, E. A new approach to calculating the memory kernel of the generalized quantum master equation for an arbitrary system-bath coupling. *J. Chem. Phys.* **2003**, *119*, 12063−12076.
(23) Shi, Q.; Geva, E. A semiclassical generalized quantum master equation for an arbitrary system-bath coupling. *J. Chem. Phys.* **2004**, *120*, 10647−10658.
(24) Zhang, M.-L.; Ka, B. J.; Geva, E. Nonequilibrium quantum dynamics in the condensed phase via the ge neralized quantum master equation. *J. Chem. Phys.* **2006**, *125*, 044106−12.
(25) Ka, B. J.; Zhang, M.-L.; Geva, E. Homogeneity and Markovity of electronic dephasing in liquid solutions. *J. Chem. Phys.* **2006**, *125*, 124509.
(26) Cohen, G.; Rabani, E. Memory effects in nonequilibrium quantum impurity models. *Phys. Rev. B: Condens. Matter Mater. Phys.* **2011**, *84*, 075150.
(27) Wilner, E. Y.; Wang, H.; Cohen, G.; Thoss, M.; Rabani, E. Bistability in a nonequilibrium quantum system with electron-phonon interactions. *Phys. Rev. B: Condens. Matter Mater. Phys.* **2013**, *88*, 045137.
(28) Cohen, G.; Wilner, E. Y.; Rabani, E. Generalized projected dynamics for non-system observables of non-equilibrium quantum impurity models. *New J. Phys.* **2013**, *15*, 073018.
(29) Cohen, G.; Gull, E.; Reichman, D. R.; Millis, A. J.; Rabani, E. Numerically exact long-time magnetization dynamics at the nonequilibrium Kondo crossover of the Anderson impurity model. *Phys. Rev. B: Condens. Matter Mater. Phys.* **2013**, *87*, 195108.
(30) Kelly, A.; Markland, T. E. Efficient and accurate surface hopping for long time nonadiabatic quantum dynamics. *J. Chem. Phys.* **2013**, *139*, 014104−10.
(31) Kidon, L.; Wilner, E. Y.; Rabani, E. Exact calculation of the time convolutionless master equation generator: Application to the nonequilibrium resonant level model. *J. Chem. Phys.* **2015**, *143*, 234110−9.
(32) Pfalzgraff, W. C.; Kelly, A.; Markland, T. E. Nonadiabatic Dynamics in Atomistic Environments: Harnessing Quantum-Classical Theory with Generalized Quantum Master Equations. *J. Phys. Chem. Lett.* **2015**, *6*, 4743−4748.
(33) Montoya-Castillo, A.; Reichman, D. R. Approximate but accurate quantum dynamics from the Mori formalism: I. Non-equilibrium dynamics. *J. Chem. Phys.* **2016**, *144*, 184104−16.
(34) Kelly, A.; Brackbill, N.; Markland, T. E. Accurate nonadiabatic quantum dynamics on the cheap: Making the most of mean field theory with master equations. *J. Chem. Phys.* **2015**, *142*, 094110−9.
(35) Kelly, A.; Montoya-Castillo, A.; Wang, L.; Markland, T. E. Generalized quantum master equations in and out of equilibrium: When can one win? *J. Chem. Phys.* **2016**, *144*, 184105.
(36) Kidon, L.; Wang, H.; Thoss, M.; Rabani, E. On the memory kernel and the reduced system propagator. *J. Chem. Phys.* **2018**, *149*, 104105−4.
(37) Pfalzgraff, W.; Montoya-Castillo, A.; Kelly, A.; Markland, T. Efficient construction of generalized master equation memory kernels for multi-state systems from nonadiabatic quantum-classical dynamics. *J. Chem. Phys.* **2019**, *150*, 244109−16.
(38) Mulvihill, E.; Schubert, A.; Sun, X.; Dunietz, B. D.; Geva, E. A modified approach for simulating electronically nonadiabatic dynamics via the generalized quantum master equation. *J. Chem. Phys.* **2019**, *150*, 034101.

https://doi.org/10.1021/acs.jpcb.1c05719
J. Phys. Chem. B 2021, 125, 9834−9852

(39) Mulvihill, E.; Gao, X.; Liu, Y.; Schubert, A.; Dunietz, B. D.; Geva, E. Combining the mapping Hamiltonian linearized semi-classical approach with the generalized quantum master equation to simulate electronically nonadiabatic molecular dynamics. *J. Chem. Phys.* **2019**, *151*, 074103.
(40) Mulvihill, E.; Lenn, K. M.; Gao, X.; Schubert, A.; Dunietz, B. D.; Geva, E. Simulating energy transfer dynamics in the Fenna-Matthews-Olson complex via the modified generalized quantum master equation. *J. Chem. Phys.* **2021**, *154*, 204109.
(41) Kubo, R.; Toda, M.; Hashitsume, N.*Statistical Physics II: Nonequilibrium Statistical Mechanics*; Springer-Verlag: New York, 1985.
(42) Zwanzig, R.*Nonequilibrium statistical mechanics*; Oxford University Press: New York, 2001.
(43) Kim, H.; Nassimi, A.; Kapral, R. Quantum-classical Liouville dynamics in the mapping basis. *J. Chem. Phys.* **2008**, *129*, 084102.
(44) Thompson, K.; Makri, N. Influence functionals with semiclassical propagators in combined forward-backward time. *J. Chem. Phys.* **1999**, *110*, 1343.

https://doi.org/10.1021/acs.jpcb.1c05719
J. Phys. Chem. B 2021, 125, 9834−9852